A THESIS
presented to
The Faculty of Division of Graduate Studies

EXPERIMENTAL VERIFICATION OF A MODEL OF A TWO-LINK FLEXIBLE, LIGHTWEIGHT MANIPULATOR

By

James David Huggins

In Partial Fulfillment
of the Requirements for the Degree
Master of Science
in the School of Mechanical Engineering

Georgia Institute of Technology

June, 1988

Acknowledgement

I wish to thank Dr. Book for his kindness, patience, and guidance while working on this project. I also wish to thank Jae Won Lee for his cooperation and advice in developing the model for the manipulator and in performing the experiments, and Dong-Soo Kwon for his work on the Finite Element Model. A number of other people have also contributed to this work. The names that stand out are Ya-Chien Chung who did early verification work, and Bau-San Yuan who is currently working on control strategies and modeling that incorporates the experimental results. This work was supported in part by the CIMS program here at Georgia Institute of Technology and in part by NASA Grant NAG 1-623. Last, but not least, I wish to thank my family and my God without whom none of this would have been possible.

TABLE OF CONTENTS

List of Illustrations

List of Tables

CHAPTER I

Introduction

The objective of this thesis is to present experimental verification of an assumed modes model of a large, two link, flexible manipulator that has been designed and constructed in the School of Mechanical Engineering at Georgia Institute of Technology. The structure was designed to have typical characteristics of a lightweight manipulator. Lightweight structures and lightweight manipulators are currently the object of much research [2,3,12,14,18] and are rapidly gaining in use. For example, the automotive industry is replacing many steel components on automobiles with aluminum or plastics and composite materials. The aircraft industry is using a number of lightweight, composite materials for construction of wings. In fact, "Composites will account for half the structural weight of the Advanced Tactical Fighter" [22]. Generally, lightweight materials are used to reduce weight so that performance is enhanced. Where possible, materials are chosen which are not only lightweight, but also have good stiffness properties. Good examples of these alternative materials include aluminum alloys in place of steel or graphite composites in place of aluminum.

The performance of robotic manipulators can also be enhanced by the use of lightweight structural members. Traditional robot manipulators have been designed for rigidity instead of strength considerations by using short arm lengths and heavy

steel construction in order to achieve positional accuracy and stability of the robot's movements. Lightweight manipulators have a number of advantages over rigid manipulators. These include lower power consumption, higher load to weight ratios, larger workspaces, and the potential for higher speed operation because of lower inertia. In addition, lightweight robots can be more easily designed as self-contained, fully mobile units or as semi-permanent units that can be easily transported. However, designing structures from the standpoint of strength considerations can lead to lightweight structures in which the flexible motions of the manipulator itself must be controlled either by control algorithms or by passive damping. Lightweight manipulators use these alternative means to achieve the stability and accuracy required.

In order to implement these control strategies effectively for lightweight manipulators, an accurate model of the robot's structure and dynamics is essential. A large amount of work has been done on modeling flexible structures and in developing controls for flexible structures [2,3,5,8,10,16]. The majority of that work has been applied to single link manipulators or to multiple link manipulators with a single flexible link [2,3,11,18]. At Georgia Institute of Technology, a large, two link, flexible manipulator has been designed and built for purposes of research on modeling methods and control algorithms useful for flexible structures. The structure consists of two ten foot links made of aluminum tubing actuated by hydraulic cylinders. This large size was chosen to represent realistically a flexible manipulator in a region of design space where it would be most competitive, since small manipulators can be more easily and economically built to be nearly rigid.

For modeling the robot arm, two methods have been used. The first method

uses an "assumed modes" model developed using Lagrangian dynamics. Each of the links is modeled as a Bernoulli-Euler beam with two vibration modes. This model has its origin in work done by Mirro [12], Book, Whitney, and Maizzo- Neto [6,8,29] in the early 1970's. Their work considered modeling and control of flexible, serially connected, two link manipulators and was also based on Lagrangian dynamics. Book also later derived the nonlinear equations of motion consisting of rotary joints that connect pairs of flexible links [7]. Sangveraphunsiri designed a single link flexible manipulator, an optimal controller for that manipulator, and performed some initial experiments [42]. Hastings performed more extensive control experiments on the same one link manipulator [2]. Other work in modeling and control of a single link, flexible manipulator has been done by Cannon and Schmitz [30]. Unlike the single link case, the derivation of the mode shapes of a multi-link manipulator is very difficult using this analytical method since exact boundary conditions are hard to determine, the mode shapes are modified by coupling forces from adjacent attached links and depend on the configuration of the manipulator and its control algorithm. The flexible closed loop chain involved in actuating the second link sets this modeling effort apart from most other efforts in the robotics or mechanism literature although Matsuno, et al, have presented work on controlling a flexible manipulator with a parallel drive [15]. This assumed modes model uses an open tree topology in describing the kinematics of the parallel link that actuates the upper link of the manipulator incorporating some of the kinematic ideas described by Singh, VanderVoort, and Likins [32]. Other kinematic principles developed by Turcic, and Midha [33,34], Sunada and Dubowsky [36], Sadler and Sandor [35] and Dubowsky and Gardner [37] were also considered in developing the assumed modes model. Preliminary work on an assumed modes model used for verification in this

thesis was done by Chung [38]. The most recent modeling effort of the two link manipulator at Georgia Institute of Technology has been done by Jae Won Lee [39]. An abbreviated derivation of his work is presented in Appendix A.

A second modeling method, a finite element model, is only used for verification of the linear aspects of the assumed modes model. Sunada and Dubowsky have applied finite element methods (FEM) to dynamic systems of coplanar links [36] and Turcic and Midha have also used the FEM methods for dynamic analysis of elastic mechanisms [33,34], however their techniques were not applied in the modeling work done here. The advantage of the finite element method is that it provides a systematic way of modeling complex geometries with linear small motion dynamics. However, because the computations used require large amounts of time, it is not practical for realtime control. Since the assumed modes model can be reduced in order by making the proper simplifying assumptions and since it includes the non-linear effects of the structure such as are encountered during fast and large motions, it is the model of choice, but requires verification. It will be the model used in other work researching control of flexible structures.

Measurement methods for verifying small motion dynamics have been in use for a number of years. Recent development of the digital signal analyzer have made linear analysis of structures much more simple than with analog methods. There are many reports on the methods used for finding eigenvalues and eigenvectors of structures. The procedures used in this thesis generally follow recommendations outlined in Ewins [26] and in Hewlett-Packard's guides to vibration testing [27,28]. Generally, a single shaker was attached to the lower link and excited with random noise. The response of the manipulator was measured

using a piezoelectric accelerometer that was moved to various locations along the links. The methods used provided both magnitude and phase information about each mode. Comparison will be made between the eigenvalues and eigenvectors measured and those predicted by the linearized assumed modes model and those found using FEM methods.

For nonlinear analysis, there are no such standard methods for analysis. The vast majority of analyses done on flexible structures thus far has been done on one link flexible manipulators [2,3] or on multilink manipulators with a single flexible link [18], although Singh, VanderVoort, and Likins have simulated dynamics of flexible bodies used in a tree topology [32] and Hughes has presented experimental work on the dynamics of a chain of flexible bodies [40]. In this thesis, time domain measurements are used for nonlinear comparisons with the assumed modes model. Occasionally, the time domain signals are transformed to the frequency domain to see if the response of the structure could be approximated by a linear system. The comparisons made will be between the actuator displacement, joint angles, and strain at the midpoint of each link.

CHAPTER II

Description of Experimental Apparatus

This robot structure was designed by a master's student at Georgia Institute of Technology for the purposes of research in control and modeling of a viable, full size, flexible robot [1]. The design parameters included the following:

1. A payload of 100 lbs.

2. Acceleration of the payload at one g.

3. To be able to reach second story windows from the ground floor.

4. Utilize two lightweight links.

To accomplish the goals of this design, the links were chosen to be ten feet long, made from round aluminum tubing. Aluminum tubing was chosen for the main structural members because of its high strength-to-weight ratio, its low cost, and its ready availability. The lower link is constructed from Schedule 10 pipe having a 5.563 inch O.D. with a wall thickness of 0.134 inches. The upper link is constructed from Schedule 10 pipe having a 4.50 inch O.D. with a wall thickness of 0.12 inches. The weights of the links without the sleeves are 26.86 lbs. and 19.40 lbs., respectively. The upper link is actuated through a "pusher" link. This "pusher" link, hereafter referred to as the actuator link, is constructed from rectangular aluminum tubing $4 \times 1.75 \times .125$ inches thick. The links are connected end to end

using thick sections of aluminum tubing. See Figure 2.1. The joints are constructed with steel pins and bronze bushings. For further details about the construction of the flexible arm see reference [1].

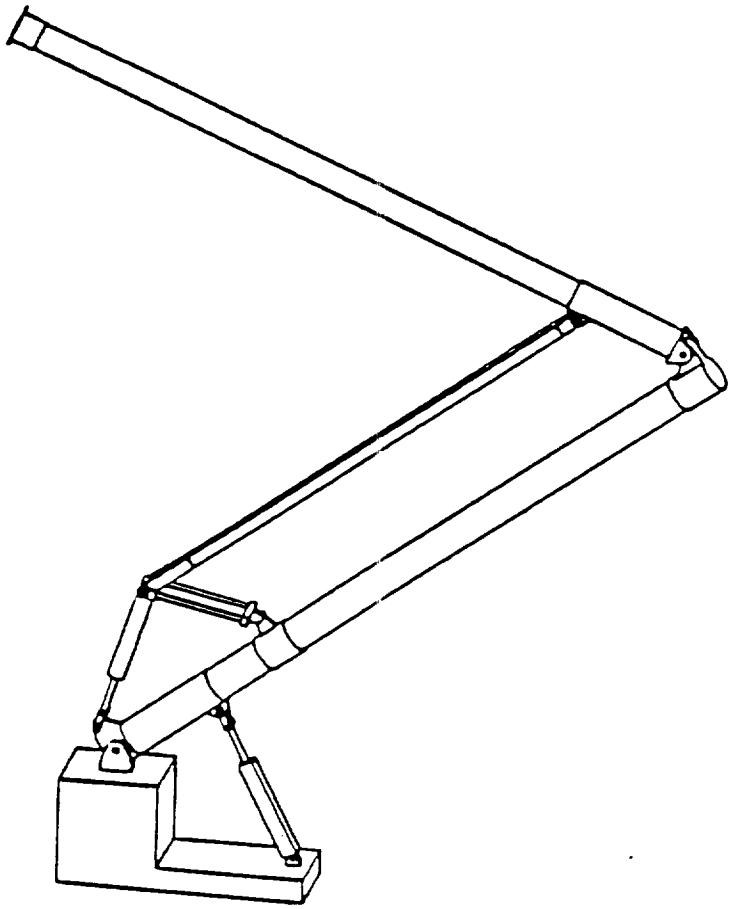

RALF
(Robotic Arm, Large and Flexible)
Figure 2.1

Both links are actuated with single ended hydraulic cylinders. The lower link is actuated directly with the cylinder while the upper link is actuated through a parallel four bar linkage. The original design was to use brushless DC motors together with ball screws to move the links, but hydraulic cylinders were used

because of the safety, the low cost of the cylinders compared to the DC motors and the ready availability of a hydraulic power unit. Use of hydraulics does introduce some nonlinearities, however the modeling of hydraulic servovalves and cylinders has been studied in considerable detail. The model used for the actuators follows the established procedures [31]. The sizes of the cylinders were chosen from the information provided in reference [1]. Figure 2.2 shows the nomenclature that will be used in the rest of this thesis. The lower link is actuated with a two inch diameter cylinder. The upper link is actuated with a 3.25 inch cylinder. The hydraulic power unit can supply 2000 psi at which the amount of force available is 6280 lbs. from the smaller cylinder and 14,140 lbs. from the larger cylinder.

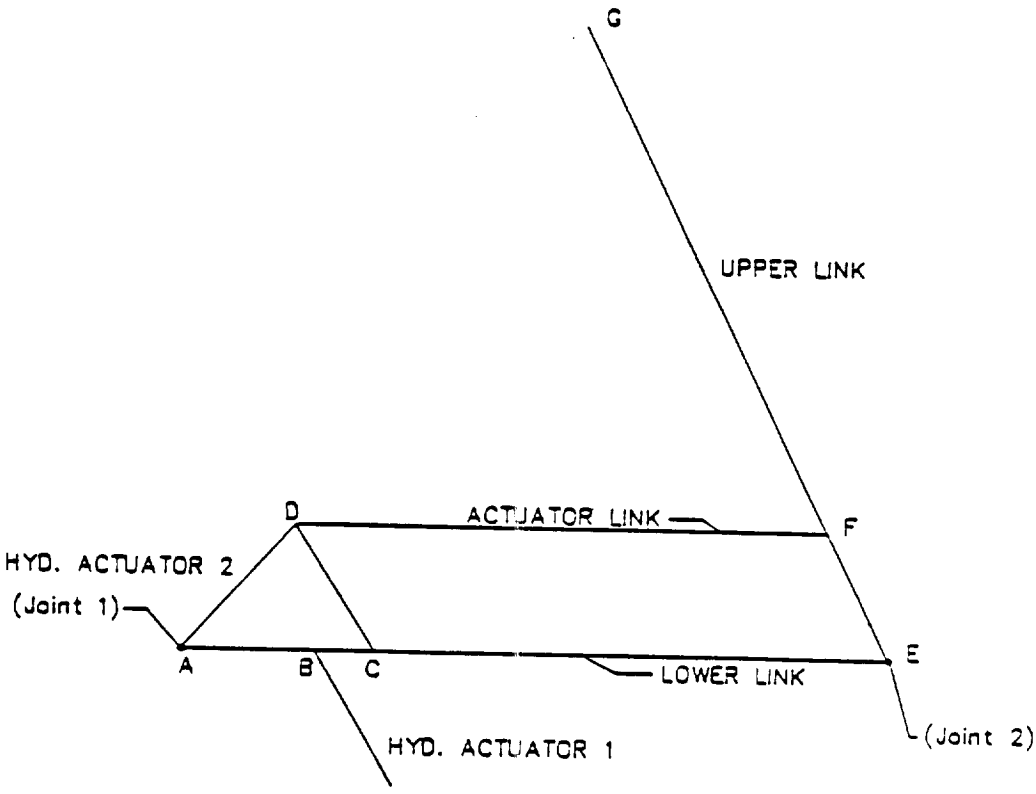

Nomenclature of Manipulator
Figure 2.2

Using hydraulic cylinders limits the range of motion of the robot. The range of the shoulder joint (Joint 1) is from 37° to 110° measured from the horizontal. The range for the elbow joint (Joint 2) is 55° to 108° when measured relative to the lower link. The range of motion for the elbow link measured from the horizontal is 92° to 145°. These ranges were chosen to provide a more interesting workspace for the experiments because the arm can cross over the vertical plane containing the axis of the shoulder joint and can reach approximately 200 inches vertically above the shoulder joint. See Figure 2.3 for the workspace depiction.

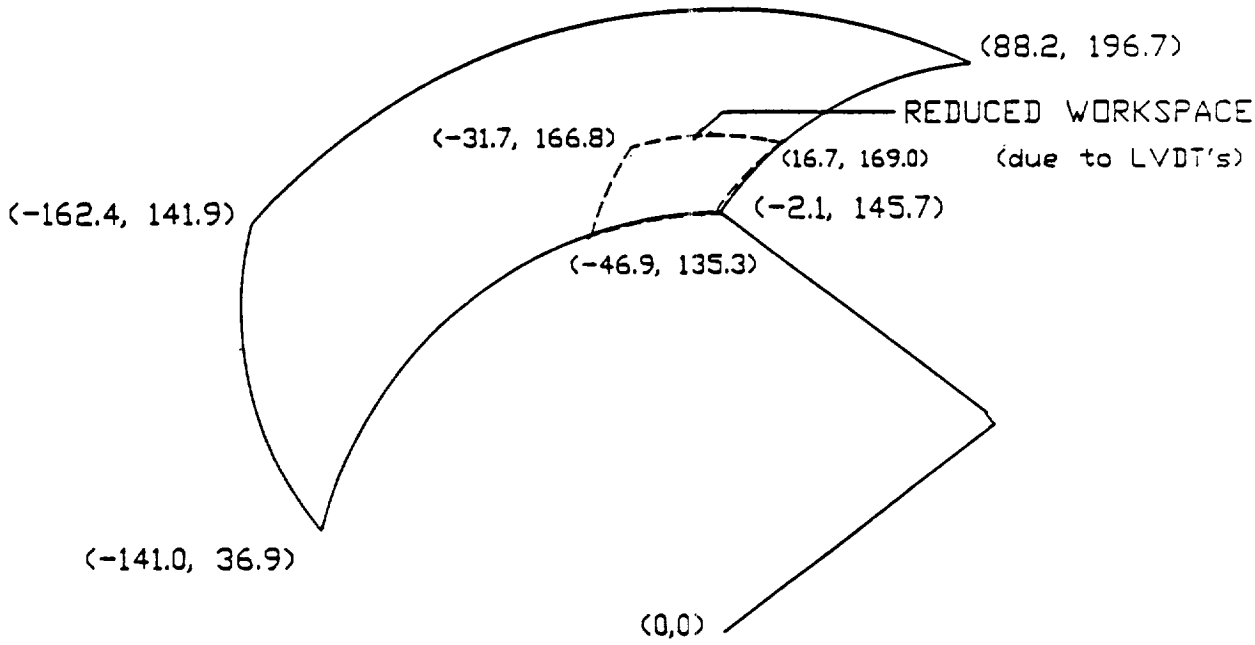

Manipulator Workspace
Figure 2.3

The hydraulic servovalves used are two stage. The first stage is a flapper valve, the second is a spool. The flow rate is 5 gpm for both valves. Therefore, the maximum linear speed for the shoulder joint actuator is 6.127 in/sec, and 8.170 in/sec, for extension and retraction, respectively. The maximum speeds for

the elbow joint are 2.320 in/sec and 3.268 in/sec, for extension and retraction, respectively. The geometric relationship of the actuator's extension to the joint angle rotation results is nonlinear as can be seen in Figures 2.4 and 2.5.

During testing of the hydraulic cylinders to determine their bandwidth, it became apparent that the position control loop was much more stable when the measurement of the hydraulic actuator's position was used for the feedback instead of the joint angle. This was caused because the joint angle measurement is not located at the same position as the actuator and because the flexibility of the link between the actuation point and the measurement point caused a 180° phase shift as soon as the structure neared the first system frequency. Figure 2.6 shows the effects of the flexible links on the measurement of the joint angle. The transducer mounted at the joint reflects the flexible motion, while the LVDT mounted on the actuator does not reflect the flexibility of the link. This necessitated the use of LVDT's for feedback of the actuator's position. The only LVDT's available on short notice were 6" long units. A large reduction in the available workspace resulted and limited the variety of experiments performed. The dotted line in Figure 2.3 shows the reduced workspace.

Digital Control and Data Acquisition

To verify the nonlinear part of the assumed modes model, it was desired to be able to move the manipulator along a prescribe path and to be able to gather data while moving. This required a number of tasks to be accomplished. First, the transducers and associated amplifiers had to be acquired. Appendix C includes a listing of these. The quantities to be measured were:

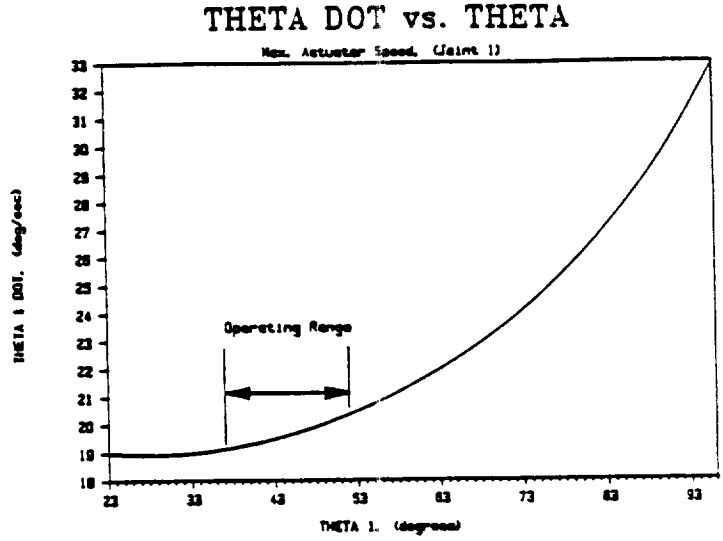

Angular Velocity vs. Angular Position, Actuator 1
(at actuator speed, 6.127 in/sec)
Figure 2.4

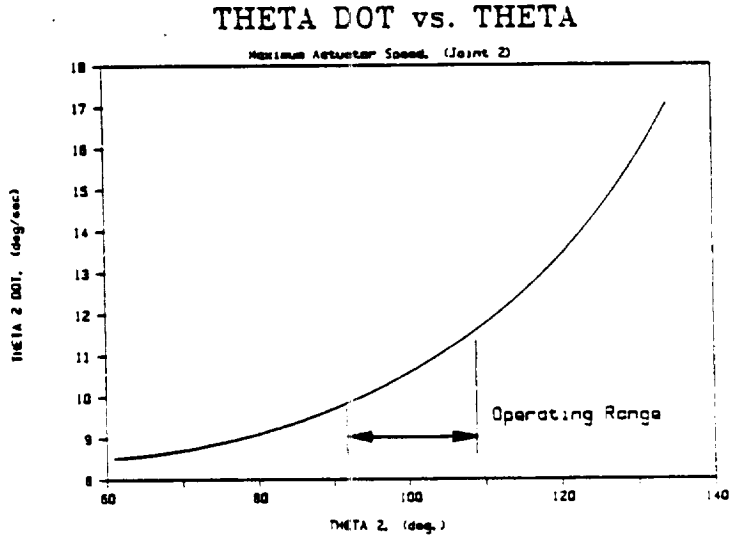

Angular Velocity vs. Angular Position, Actuator 2
(at actuator speed, 2.32 in/sec)
Figure 2.5

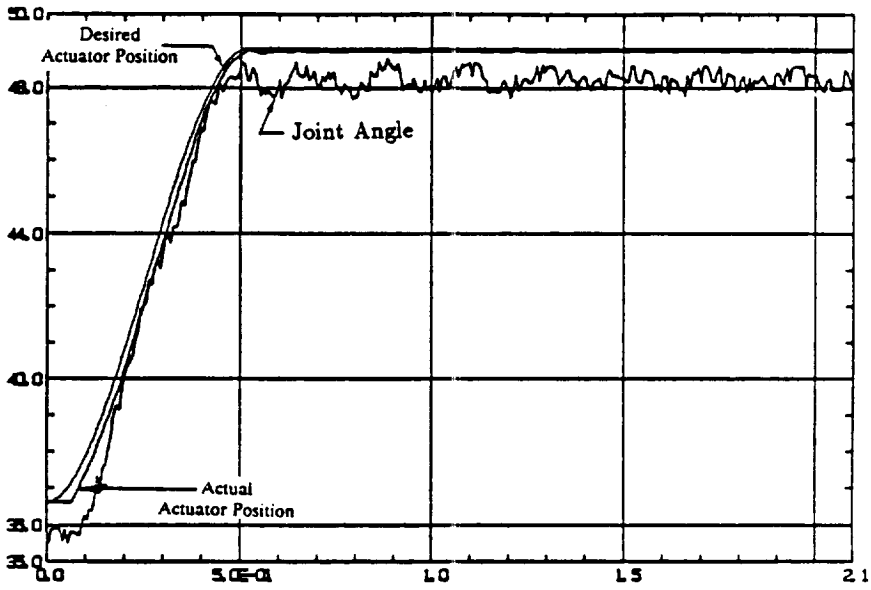

**Joint Angle Transducer vs.
Actuator Length Measurements**
Figure 2.6

1. Joint angles

2. Joint velocity

3. Strain in the links

4. Actuator displacement

5. Acceleration of points on the links

6. Differential pressure in the actuator

All transducers with the exception of the LVDT's and the accelerometers were purchased as new components. These transducers were installed on the existing

manipulator and tested using a simple analog controller. (All output from these transducers is in analog form.)

Next, to be able to control the manipulator and gather data from multiple sensors simultaneously, control was switched to a Digital Equipment Co. Microvax II. The necessary analog/digital (A/D) board was purchased from Data Translation. The A/D board came with compiled software routines that could be linked to programs written in Fortran. Therefore, the entire program for control and data acquisition was written in Fortran. This was written in modular form so that the other students in our research group could easily add other path planning and control algorithms. Appendix D describes the computer programs in greater detail.

The program was then tested for speed. In order to effectively implement the control algorithm, it was necessary to know the speed at which the A/D board could read the eight input channels and output a value on the D/A channel. It was found that the A/D board could reliably sample a single channel at 6000 Hz. Eight channels could be reliably sampled at only 300 Hz. When the control algorithm's computations were added to the loop between the data's acquisition and the control output, the frequency of the sampling rate went down to approximately 150 Hz. It should be noted that the 150 Hz rate was used for all control used in testing the manipulator, regardless of the amount of data required for any particular test. This allows consistent path planning to be done. A second A/D board is available on the Microvax, but a 1 millisecond delay is required when switching control from one board to the next. The second A/D board was not used in any of these experiments.

Initial verification of the system frequencies and mode shapes was made with

a two channel digital analyzer. A second verification was made using software from Structural Dynamics Research Corp. (SDRC) called **Tdas**. To utilize this software, Fortran programs were written to gather and catalog time response data from which frequency response functions (FRF's) could be calculated. Then, these data files were converted to **Tdas** readable format by writing a subroutine that could be linked with an SDRC provided program. After the files had been converted, the software could be used to create a file containing all the FRF's for the measurement points on the manipulator and to quickly generate the mode shapes and system frequencies.

This conversion of data files also proved to be useful later when comparing the results of the experiments and the results of the assumed modes model. By choosing an appropriate file format, data could be sent over the campus network to the computer where the manipulator's dynamics were being simulated. The predicted results could then be compared directly with the measured results and plotted together. Figure 4.3 is an example of this.

CHAPTER III

Linear Modeling, Test Methods and Results

The first step taken to verify the model was to test the linear vibration characteristics of the structure. The linear behavior for small motions about an operating point is one of the most practical comparisons to make between a dynamic system and its model. For vibrational systems with light damping, this is equivalent to comparisons of the natural frequencies, damping ratios, and system mode shapes. This chapter compares the eigenvalues and eigenvectors found from the linearized assumed modes model and from two FEM (finite element method) models with those experimentally measured. Since the assumed mode shape model results in a drastic reduction in order from either the real system or the finite element model, this is especially important for verification of that modeling method. Other analytical methods, such as a balanced realization [23], have been applied to choosing the model order but these methods assume the high order model to be perfect. This structure is complex and imperfect, so that experiments to determine the system parameters are essential. A detailed discussion of the modeling methods and the experimental methods used follows.

Linearized Assumed Mode Shape Model

The following is an excerpt from work done by Jae Won Lee, a PhD. candidate at Georgia Institute of Technology. It is included here for completeness.

A more thorough derivation of the assumed modes modeling method is included in Appendix C. The equation numbers used here refer to the numbers used in the appendix. The equations of motion have been derived through application of Lagrange's equations. The assumptions used by the linearized assumed modes model are as follows:

1. All pin joints are perfect, ie., there is no friction in the joints.
2. The structure is perfectly aligned.
3. There is no mechanical looseness or slop in any part of the structure.
4. The hydraulic actuators behave as rigid members.
5. The joints of the links are connected at the centerline of the adjoining links.
6. The lower link segments $\overline{AB}$ and $\overline{AD}$ are rigid. See Figure 2.2.
7. The upper link segment $\overline{EF}$ is rigid. See Figure 2.2.
8. The area moment of inertia is constant along the entire length of the link.
9. The boundary conditions are:
    a. Clamped-mass for the lower link.
    b. Clamped-free for the upper link.
    c. Pin-Pin for the actuator link.
10. The structure vibrates only in the plane formed by the two links.

11. The structure behaves linearly.

12. The constraint equation includes only the bending of the lower beam.

The eigenvalues and eigenvectors are obtained from the equations of motion of the reduced equations (A.2.21) linearized about zero velocity.

$$V_2^T M V_2 \ddot{z} + V_2^T K V_2 z = 0 \tag{A.3.1}$$

Eigenvalues of (A.3.1) are the same as those of the constrained equation (A.2.7). Eigenvectors of the constrained system are derived by transforming those of (A.3.1) using

$$q = V_2 z. \tag{A.3.2}$$

For numerical analysis, the selection of mode shape functions is necessary and may greatly influence the results. In previous work [10], the natural frequencies were derived by the flexible part of the unconstrained equations:

$$M_{ff}\ddot{q} + K_{ff}q = 0 \tag{A.3.3}$$

but more accurate results were obtained by considering that the lower link bending is affected by the actuating link's rigid motion. The constrained dynamics including the actuator link motion is needed. When the actuators are fixed, velocities of joint 1 and joint 2 are zero. New constraint equations between joint 3, joint 4 and the elastic coordinates are needed. The elements of the mass matrix related to joint 1 and joint 2 (columns 1 and 2; rows 1 and 2) are deleted. The dynamic equation can then be rewritten as

$$\bar{V}_2^T \bar{M} \bar{V}_2 \ddot{Z} + \bar{V}_2^T \bar{K} \bar{V}_2 Z = 0. \tag{A.3.4}$$

From these equations, the natural frequencies are calculated. Eigenvectors are obtained by the transformation, $q = V_2 Z$.

Finite Element Method

The finite element method is a very useful method especially when it is necessary to reconcile the discrepancies between the theoretical model and the real system due to the theoretical model's simplifications. Since the parameters of the theoretical model can be easily changed to reflect various degrees of model reduction, several sets of parameters can be used in order to determine the amount of simplification necessary. In a complex multi-link system, the exact boundary conditions are unknown, so that there is no absolute basis for assuming any mode shapes for the links. The finite element model provides a method of choosing the proper boundary conditions because the dominant mode shapes of each link can be found from analysis of the system modes.

In this dynamic FEM analysis, the large flexible manipulator was modeled using linear isotropic three dimensional beam elements and lumped mass elements. Therefore, the model allows flexural and axial vibrations in all three axes directions. For boundary conditions, the ends of the hydraulic actuators were fixed to the ground by pin joints, so that these joints have zero translational displacements and only allow rotation about the z-axis. Figure 3.1 shows the nodes and grounding points used. All beams and links are connected with pin joints using idealized coupled constraints. To describe the pin joints, the coupled constraint conditions allow only one rotational degree-of-freedom about the z-axis between the coupled nodes at the joints [24]. When only two dimensional motion was analyzed, the

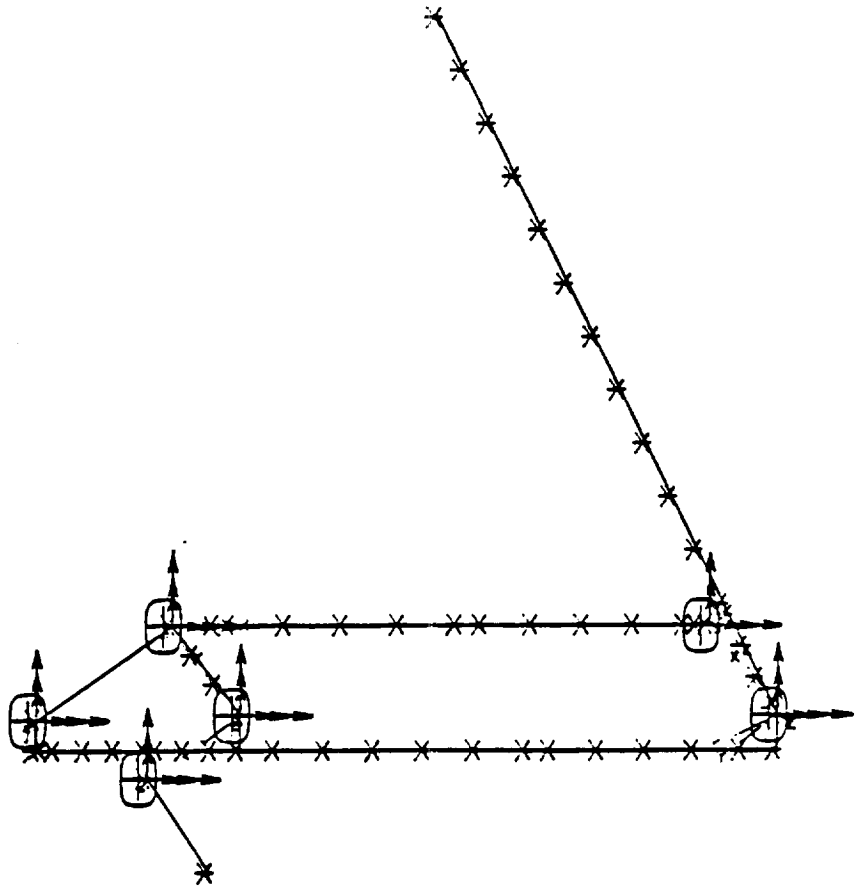

Nodes of the Finite Element Model
Figure 3.1

z-axis translational degree-of-freedom and the x and y axes rotational degrees-of-freedom were restricted by nodal displacement restraints [24]. The hydraulic actuators were modeled as rigid links. The Coulomb friction at the joints and the structural damping of the beams were ignored in the dynamic analysis. For dynamic analysis, the simultaneous vector iteration method was used to obtain the natural frequencies and system mode shapes [25].

Two types of finite element models were created: one is a simplified model using beam elements with seven different EI (modulus of elasticity, area moment of inertia) values and one lumped mass element using the same physical dimension data and rigidity assumptions as used in the assumed modes model. The other

model uses more detailed dimensional data. Beam elements with thirteen different EI values were used along with three kinds of lumped mass elements so that it more closely matches the actual structure. The second model makes no assumptions about the rigidity of any of the links – only the hydraulic actuators are assumed rigid. In particular, the more detailed model uses exact EI values along the length of the beam to account for the manipulator's support sleeves whereas the simplified model uses a single EI value for the entire length of the beam. The detailed model also takes into account the fact that the links are not connected at the centerlines, but are connected with offset brackets and includes every lumped mass on the manipulator, even the larger steel bolts used for assembly. These two FEM models can be used to explain the discrepancy between the assumed mode method and the results of the experiment.

Experimental Procedures for Linear Vibration Analysis

Literature on vibration testing [26,27] suggests that certain types of input are more appropriate than others, particularly when the structures exhibit non-linear behavior. Therefore, each of the suggested input methods was tried. The methods tried were step relaxation, impact hammers, random noise, burst random noise, swept sine, periodic burst chirp, and exciting the structure with the hydraulic actuators themselves. Since all of the input methods yielded similar information about the eigenvalues, random noise using the electromechanical shaker became the input of choice because of its ease of use, its ability to excite the higher frequencies, its accuracy, the ability to gather phase information as well as frequency information, and the ability to measure the coherence of the signals. Exciting the

structure with the hydraulic actuators was judged to be not as accurate as exciting the manipulator with the shaker because of the response of the actuator caused a small shift in the frequencies measured and because the input force to the structure could not be measured directly.

To verify the small motion dynamics, an electromechanical shaker was attached to the structure at the second joint (Point E in Figure 2.2). The structure was excited in the frequency range from 1 to 500 Hz. For more detailed information about particular system frequencies, the input frequency range to the shaker was narrowed to provide better accuracy. The input of the shaker was measured by a piezoelectric force transducer installed between the shaker and the lower link. The response, acceleration, was measured by a piezoelectric accelerometer. Since the force transducer was mounted on the structure at the point of application of the shaker, the frequency responses obtained can be attributed only to the shaker input and are independent of any coloration of the dynamics of the electronic driver of the shaker. The weight of the force transducer is approximately 25 grams. Its effect on the response of the structure is judged small enough to be insignificant.

To measure the eigenvectors associated with the eigenvalues, each link was marked in 6 inch increments. The accelerometer was mounted at the marked positions in the plane of links and perpendicular to the links. Figure 3.2 shows the location of the measurement points along the links of the manipulator and Figure 3.3 shows the typical placement of the accelerometer at each point. The structure was then excited with the electromechanical shaker and 30 averages of the frequency response were taken to minimize noise effects. The frequency response measurements were calculated using the cross spectrum function [28]. This method

provides both magnitude and phase information. The correlation of the two signals was checked at each measurement point. The frequency response function was then integrated twice using the math functions of the digital frequency analyzer to obtain a plot of displacement/input force (compliance). As outlined in the Hewlett-Packard guide [27] to vibration measurements, the mode shape can be found by measuring the imaginary part of the frequency response (provided the structure has only proportional damping) at each point along the beam then plotting its magnitude.

The eigenvalue/eigenvector measurement procedure was done twice. The first measurements were made using a two channel digital frequency analyzer. This was a time consuming procedure because of the number of measurement points used to measure the mode shape and because the existence of the out of plane vibration modes caused some uncertainty in the measurements. The low frequency vibration modes were clearly separated, but the higher system frequencies were obscured because of their small magnitude, the out of plane modes and the closeness of the frequencies. See Figure 3.4.

The second set of data was gathered using a Microvax II and an A/D board. This allowed gathering time history data directly from multiple points on the structure. Using software from the Structural Dynamic Research Corporation (SDRC), the time history data was converted to frequency response data. This made the task of determining the mode shapes became much easier because the software can automatically generate the mode shapes from a series of frequency response functions (FRF) stored in the computer.

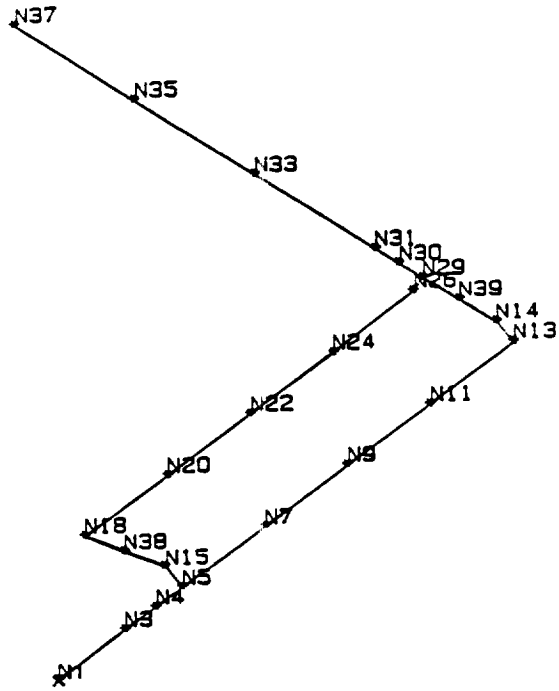

Experiment's Measurement Points
Figure 3.2

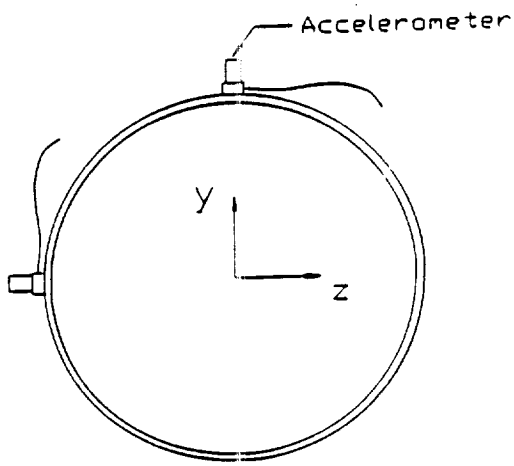

Accelerometer Position
Figure 3.3

Discussion of Results of Linear Analysis

Table 3.1 shows a comparison of the system frequencies obtained from each of the modeling methods.

Table 3.1

System Frequencies

Assumed Modes Model	Simplified FEM Model	Detailed FEM Model	Exper. Results	Damping Ratio
6.21	6.03	5.95	6.37	.008
16.90	15.24	12.78	12.00	.013
30.76	30.74	30.19	37.87	.007
95.40	75.63	60.60	57.37	.026
98.25	104.60	95.05	94.02	.019
120.70	120.28	115.00	120.20	.005

The first three system modes were easily determined because of their clear separation from the other frequencies, but higher frequencies become increasingly difficult to analyze because of their much smaller amplitude and the closeness of the eigenvalues. Figure 3.4 shows a typical inertance driving point plot of the measured frequency response function (FRF). When analyzing the manipulator with the two channel analyzer, the comparison of the experimental results with the theoretically predicted modes was very useful. The fourth and fifth modes were obscured by the out of plane vibrations. The fourth mode was originally overlooked due to its small magnitude. By comparison with the finite element model, the fourth mode was clearly shown to be dominated by the vibration of the lower link and that there was an out-of-plane system mode at a slightly higher frequency. Subsequent measurements confirmed both the 57.37 Hz in-plane mode and an out-of-plane mode

Driving Point FRF (inertance)
Figure 3.4

at 63 Hz.

Without the theoretical predictions of the natural frequencies and mode shapes, it would have been very time consuming to find the higher frequency mode shapes, especially since the manipulator being examined here has a number of out-of-plane frequencies that are nearly the same frequency and magnitude as the in-plane vibrations. Even with the use of the FEM model to help determine the system frequencies, the original determination of the mode shapes was found to have some small errors in the higher order modes primarily due to the presence of out of plane vibrations. Using the SDRC software and the automated method for computing the system mode shapes yielded more accurate results than were obtained using the two channel analyzer because the complex interaction of the modes of the structure

at higher frequencies could be displayed rapidly. Table 3.1 shows a comparison of the eigenvalues obtained from each of the modeling methods. Figure 3.5 shows the mode shapes of the manipulator and the associated system frequencies.

As can be seen in Figure 3.5a, the first system mode, at 6.37 Hz, is dominated by the first bending mode of the lower link. By using clamped-mass boundary conditions, both analytical methods accurately predict this natural frequency and mode shape. The second system mode is dominated by the first bending mode of the upper link as seen in Figure 3.5b. Using clamped-free boundary conditions in the assumed modes model and using the simplified finite element model, there was a 4 Hz discrepancy with the experimental results. When the lower link's geometry was modeled more accurately in the detailed finite element model, there was much better agreement of this method with the experimental results. It is seen, then, that the simplified FEM model (using the same boundary conditions as the assumed model) agrees well with the assumed modes model and that the detailed FEM model, using no boundary condition assumptions, agrees well with the experimental results.

The largest discrepancy between the experimentally determined and the theoretically predicted natural frequencies occurs in the third and fourth system modes. The third system mode is dominated by the pin-pin bending mode of the actuator link, but unlike the first two modes, there is nearly a 7 Hz (19%) discrepancy between the measured and predicted natural frequencies. However, as can be seen in Figure 3.5c, the mode shapes from all three methods correspond well. The explanation for this is that the third mode primarily involves the vibration of the actuator link. Initially, a turnbuckle with no bearing was used in place of the upper link's hydraulic actuator, which is believed to have caused a large amount of

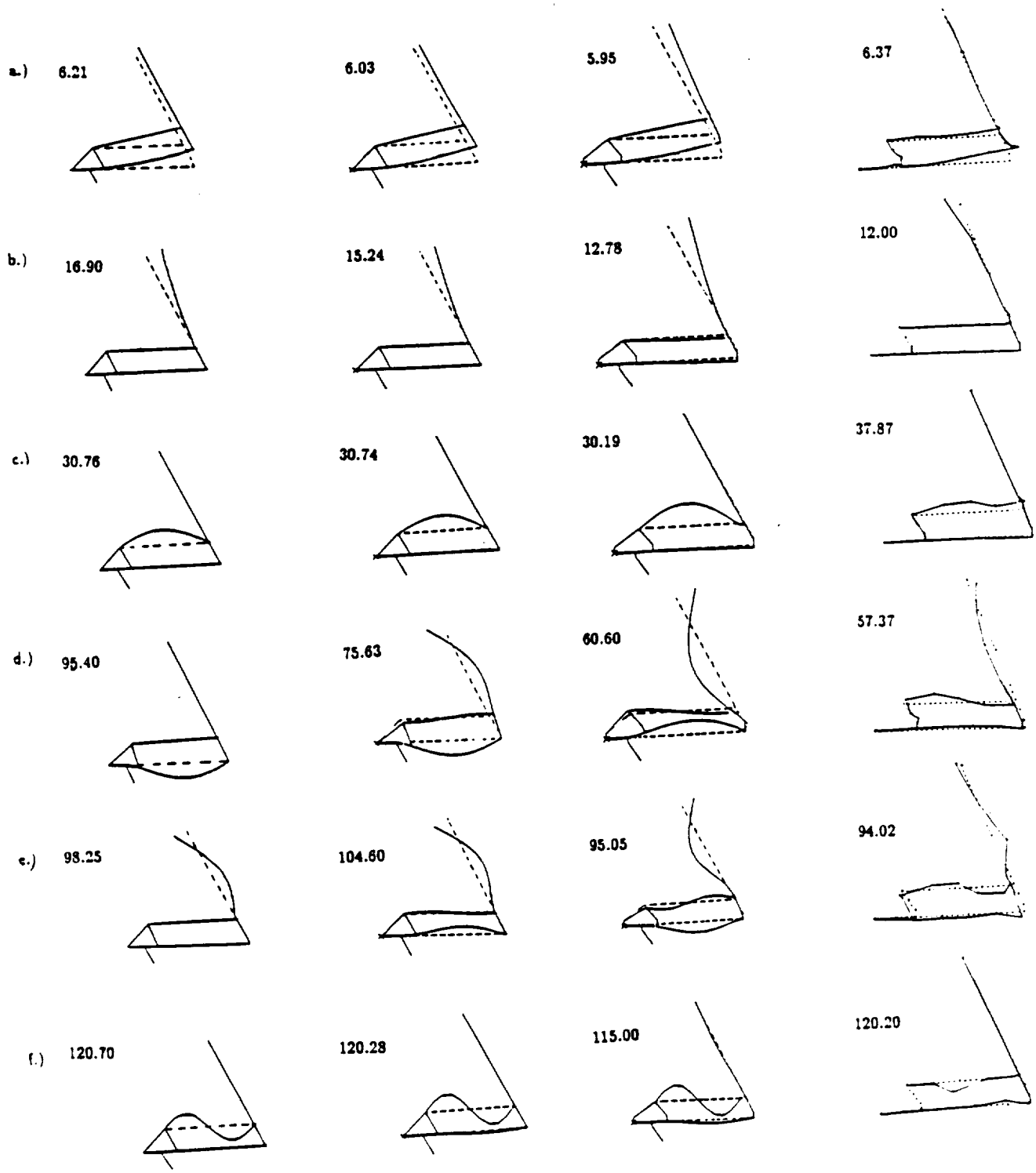

System Mode Shapes

Figure 3.5

friction in the pin joint causing the joint to exhibit some characteristics of a clamped end condition. (The finite element method modeled the link to accurately reflect the properties of a turnbuckle rather than those of a hydraulic actuator.) Using the FEM method, pin-pin, clamped-pin, and clamped-clamped boundary conditions were used for the actuator link. The resulting natural frequencies were 30.1, 46, and 64 Hz, respectively. From this, it is concluded that the difference between the measured natural frequencies and the predicted ones is most probably due to the friction in the joints of the actuator link.

In the fourth system mode, there is a 6 Hz (10%) discrepancy between the measured natural frequency and the frequency predicted by the more detailed finite element method. In Figure 3.5d, it can be seen that the fourth mode also involves the movement of the segment on the lower beam, $\overline{AB}$. Note that the 57.37 Hz fourth mode is not predicted accurately by the assumed modes method. The reason for this is that the assumed modes method models this section of the lower link as rigid and therefore ignores the movement of the lower part of the lower link. Since the fourth mode's movement is dominated by the bending of the lower link, the assumed mode method cannot predict this mode accurately. When the simplified finite element model was adjusted to reflect the same assumptions used in the assumed modes model, the results of these two theoretical methods agreed well. See Table 3.1. The assumed modes model has been improved to represent these effects but with much increased complexity. The fact that one of the system's modes was completely missed by the assumed modes method shows the importance of verifying theoretical results with experiments. In this case, the effect of the fourth system mode is small in terms of displacement and it does not significantly affect the movement of the

structure. However, the general assumption cannot be made that the higher order modes are unimportant or that they can be neglected.

The fifth system mode, Figure 3.5e, shows that the vibration of the manipulator is dominated by the second bending mode of the upper beam. This mode is predicted by both the theoretical methods and corresponds well with the experimental results. The sixth mode also agrees well among all modeling methods and experiments.

The agreement between the three methods of analysis is substantiated by the similar mode shapes found. Figure 3.5 shows normalized mode shapes of the structure, but it should be noted that the displacement of the endpoint of the upper link is of the same order of magnitude for both the first and second modes of vibration, while the third, fourth, fifth, and sixth's modes effect on the endpoint of the upper link are more than two orders of magnitude smaller than the effect of the first two modes. Therefore, for this manipulator, the control of the first two modes of the system should be of primary concern to the control designer.

Change of System Frequencies with Payload and Configuration

Large, fast motions of the manipulator can result in significant changes in configuration. Changes in payload can also dramatically affect the system frequencies. A final experimental observation was made in the changes in the system frequencies caused by changes in payload and in configuration in preparation for verifying the model for nonlinearites. All previous discussion on system modes and frequencies were based on a single configuration with no payload. This was mainly due to the fact that the structure is so large as to present problems in mounting

the electromechanical shaker and accelerometer and because the first two system modes are more clearly separated with light payloads. The results are summarized follows:

1st System Mode

1. The frequency decreases as payload increases - 6.25 Hz to 3.25 Hz.
2. The frequency decreases slightly as the manipulator opens - 6.25 Hz to 6.0 Hz.
3. The frequency decreases as the joint 1 angle increases - 6.25 Hz to 4.25 Hz.

2nd System Mode

1. The frequency decreases as payload increases - 9.75 Hz to 5.0 Hz.
2. The frequency is lowest for any given payload when the two links are at right angles to each other.
3. The frequency remains nearly constant for any given payload when only joint 1 is moving.

3rd System Mode

1. The frequency decreases only slightly regardless of payload or configuration.
2. The frequency decreases slightly as the manipulator moves to a more open configuration - 39 Hz to 36 Hz.

4th System Mode

1. The frequency decreases slightly as the payload increases - 57 Hz to 52 Hz.
2. The frequency changes little with configuration changes.

5th System Mode

1. The frequency decreases with payload - 94 Hz to 79 Hz.
2. The frequency decreases as the manipulator opens - 94 Hz to 84 Hz.

6th System Mode

1. The frequency decreases with payload - 120 Hz to 108 Hz.
2. The frequency decreases as the manipulator moves to a more open configuration - 120 Hz to 106 Hz.

3. The frequency decreases as joint 1 increases – 120 Hz to 110 Hz.

These results are generally expected from vibration theory. Increased mass decreases the system frequencies in every case. Also, increased length decreases the system frequencies because the center of gravity of the manipulator is farther from joint 1. This effect is seen in all the modes and especially in the first system mode when payloads are small. As the payloads become larger, the first system mode rate of change becomes significantly smaller relative to the rate of change in joint 1. In fact, as the payloads increase, the rate of change of all system frequencies becomes much smaller. The most dramatic changes occur in the first two system modes. These are the dominant modes for the system in that these two modes most greatly affect the motion of the endpoint. All other system modes effect on the endpoint position are more than two orders of magnitude smaller than the effect of the first two system modes.

CHAPTER IV

Non-linear Modeling, Test Methods and Results

To verify the non-linear aspects of the model, i.e., Coriolis and centrifugal effects, large scale, fast motions are needed. To accomplish these motions, control of the manipulator was implemented on a Microvax II. This computer was also used to gather data during the motion. To compare the results of the experiments to the assumed modes model's results, identical movements were programmed for each. Time domain measurements of the joint angles, actuators lengths, actuator pressure, and strain in the midpoint of each link were used for comparison.

Hydraulic Actuator

As a more detailed model of the manipulator was developed, a more accurate model of the hydraulic actuators was needed in order to accurately simulate the time response of the manipulator. Texts on hydraulic modeling [31] suggest that a third order model of hydraulic actuators is sufficient describe their response up to their bandwidth even though the actual order is considerably higher. Two series of tests were made to measure the response of the cylinder position to a swept sine input. The tests included the open loop response, the closed loop response, and the closed loop stiffness response. The procedures used closely follow test methods outlined in Merritt [31]. The first series of tests were made with the actuator detached from the structure. A second series of tests were made with the actuators attached

to the structure. A simple proportional only analog controller was used for the position loop control. A gain was chosen that would give a margin of stability and an appropriate bandwidth. This same gain was then used for all subsequent tests. When the digital controller was implemented on a Microvax II computer, an equivalent gain was chosen so that experimental results could be directly compared to the simulation results. Table 4.1 summarizes the results of these tests of both actuators when attached to and detached from the manipulator. It should be noted that these tests resulted in a linear model of the actuators. The transfer functions for each actuator were found using curve fitting of the Bode and Nyquist plots. The equations representing Joint 1 and Joint 2 closed loop actuator dynamics are, respectively, as follows:

$$H_1(s) = \frac{1}{(s + 30.37)(s + 9 \pm j16.5)} \tag{4.1a}$$

$$H_2(s) = \frac{1}{(s + 33.57)(s + 21 \pm j23.07)} \tag{4.1b}$$

Table 4.1

Summary of Actuator Tests

	Joint 1 Actuator		Joint 2 Actuator	
	detached	attached	detached	attached
Open Loop Gain	127.8	79.6	72.2	51.7
Closed Loop Bandwidth	18.6 Hz	17.8 Hz	18.8 Hz	17.2 Hz
Gain Margin	8.6 db	10.6 db	7.5 db	14.6 db
Phase Margin	41.1 deg.	31.3 deg.	59.8 deg.	64.9 deg.

Figure 4.1 shows the closed loop Bode plots of the response of the Joint 1 actuator to the swept sine input both when attached to and when detached from the structure. The similarity of these plots shows that the structure's influence on the response of the cylinder is small. That is, at the point of attachment, the manipulator follows the movement of the actuator very closely. Figure 4.2 shows the actual response of the cylinder verses the response computed from a third order curve fit. The plots are very similar up to the bandwidth of the actuator. The Bode plots for the second joint actuators also show good agreement. Graphs for the Joint 2 actuator are included in Appendix B.

Simulation Results vs. Experimental Results

Because the low frequency motion of the arm is dominated by hydraulic actuator dynamics, the time response of the gross motion of the arm can be derived from the frequency response of hydraulic actuator. The calculated time response of this transfer function for a sine input and an arbitrary input function match with the measured actual path as shown Figure 4.3.

Assumed Modes Model

This following is a continuation of the derivation included in Appendix A. The equation numbers used refer to those used in the Appendix. The flexible motion of the arm is excited by acceleration of the joints. The flexible dynamics are derived from (A.2.16)

$$V_2^T M \ddot{q} + V_2^T K q = V_2^T Q \qquad (A.2.16)$$

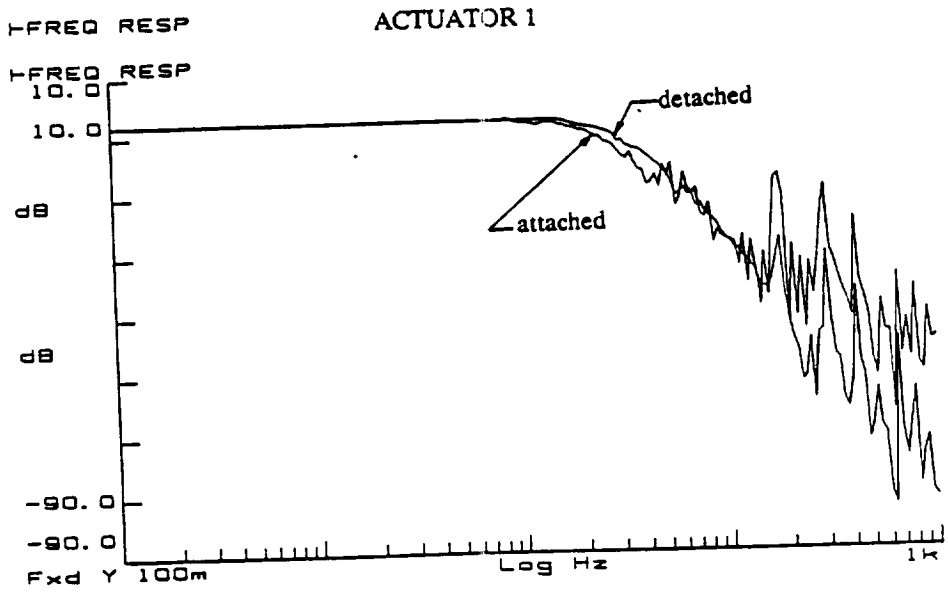

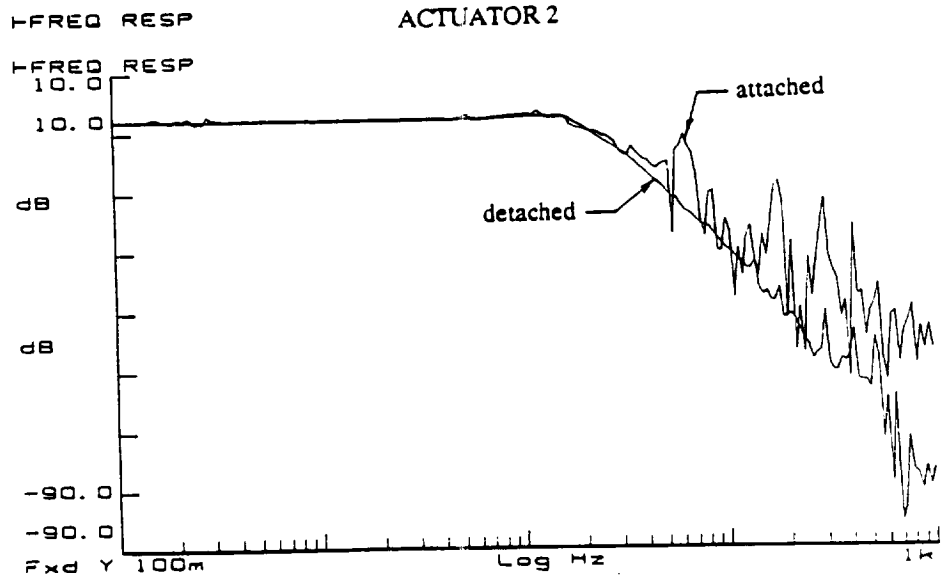

Bode Plots of Actuators 1 and 2
(when attached to and detached from the structure)
Figure 4.1

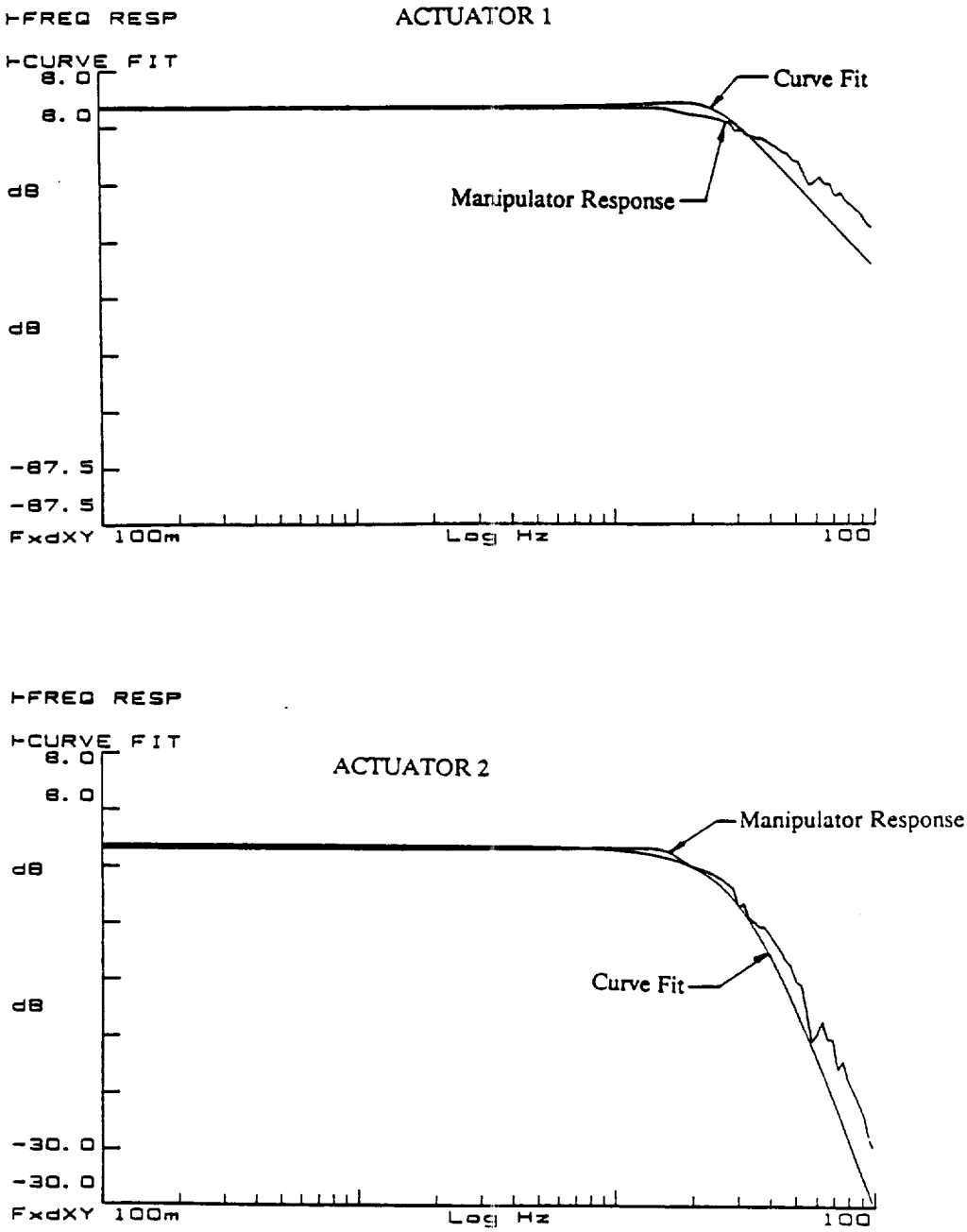

Response of Actuators vs. 3rd order Model
Figure 4.2

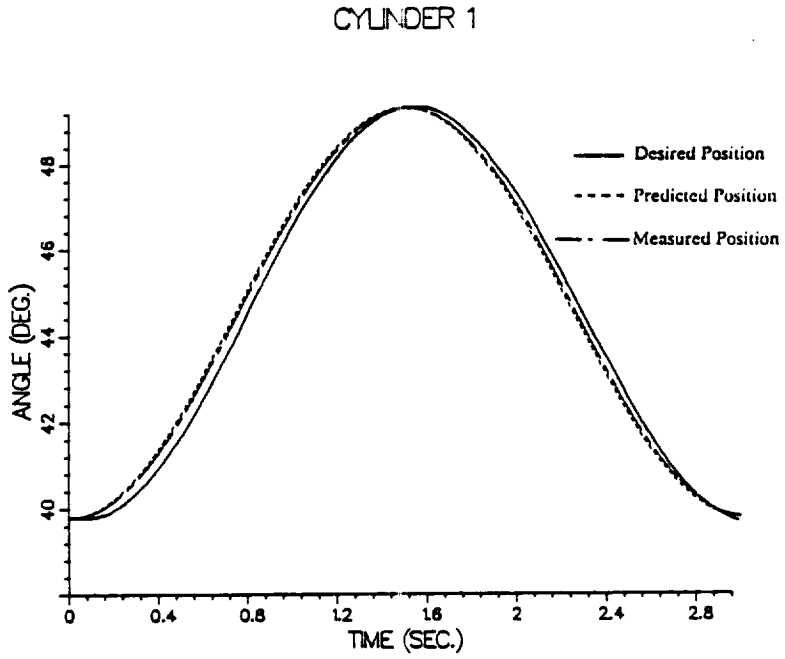

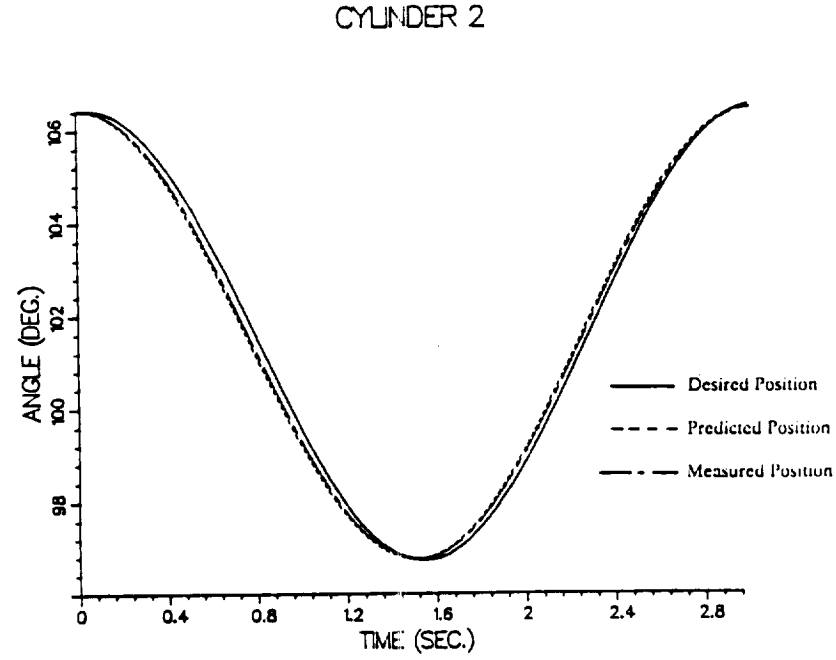

Low Frequency Time Response, Predicted and Actual
Figure 4.3

or

$$\begin{bmatrix} \underline{M}_{rr} & \underline{M}_{rf} \\ \underline{M}_{fr} & \underline{M}_{ff} \end{bmatrix} \begin{bmatrix} \ddot{q}_r \\ \ddot{q}_f \end{bmatrix} + \begin{bmatrix} 0 & \underline{K}_{rf} \\ 0 & \underline{K}_{ff} \end{bmatrix} \begin{bmatrix} q_r \\ q_f \end{bmatrix} = \begin{bmatrix} Q_r \\ Q_f \end{bmatrix} \qquad (A.2.17)$$

Flexible motion can be derived as:

$$\underline{M}_{fr}\ddot{q}_r + \underline{M}_{ff}q_f = \underline{Q}_f \qquad (4.2a)$$

or

$$\underline{M}_{ff}\ddot{q}_f + \underline{K}_{ff}q_f = \underline{Q}_f - \underline{M}_{fr}\ddot{q} \qquad (4.2b)$$

where $\ddot{q}_r$ are the accelerations of the desired path.

Experimental Methods

A variety of movements of the manipulator were used for verification. First, the response to a step input was examined to measure the transient dynamics. Next, continuous movements that were sinusoidal in joint space were used to measure steady state response. Both the amplitude and the frequency of the sinusoidal movements were varied in order to compare the experimental results with the predicted results. In both cases a single link was moved first while holding the other link fixed. Then both links were moved simultaneously. All of the tests were made with no payload because the first two system modes are more clearly separated with no loading.

During the movements of the manipulator, the following measurements were made:

1. Joint angles
2. Displacement of the cylinders (LVDT)
3. Differential pressure in the cylinder
4. Strain at the midpoint in each link

Due to the high gains used to increase the closed loop bandwidth, small disturbances, such as quantization error, had a large effect on the movements and measurements made. The analytical model assumes that there are no disturbances and that the structure is ideal. This is never the case with actual systems. The effect of each disturbance can be seen in the measurement of the bending strain. In this section, these discrepancies will be examined and their causes explained. The agreement of the model with the experimental results will also be examined.

To compare the actual movements with the simulated results, the primary measurements were the displacements of the cylinders and the strain measurements. The displacement measurements show the rigid body motion. The strain measurements show the flexible motion. Figure 4.4 shows a typical plot of the experimental measurement of strain in the lower link in which the effects of the flexible motion can be clearly seen.

Discussion of Results

In the following figures, a comparison of the results is shown for one cycle of motion. As might be expected, there were some discrepancies between actual and predicted results. However, the results showed similar trends and the discrepancies can be explained. Generally, the measured strain in the lower link matches the strain predicted. The results for the upper link do not match as closely because there are no simple theoretical boundary conditions that match the actual boundary conditions and because only two mode shapes are used. Figure 4.5 shows the strain in links when both links are moving.

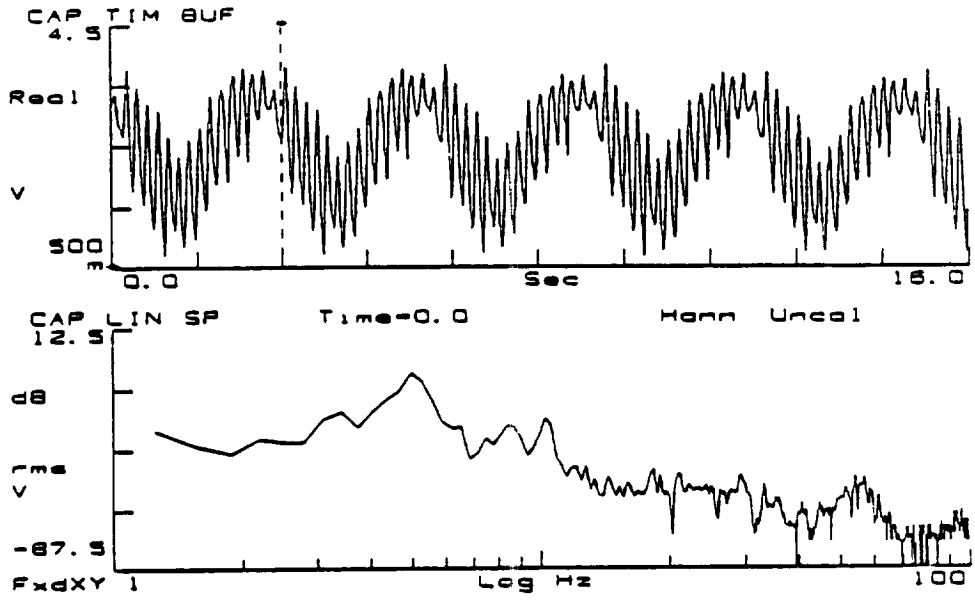

Typical Strain Measurement in Lower Link
Figure 4.4

In Figures 4.5a and 4.5b the strain in the lower link has the same general shape in both the experimental and theoretical results except for the disturbance at the peak of the movement. Both plots show that there is little damping in the lower link and that the vibration of the upper link has little effect on the vibration of the lower link. The disturbance in the measured strain was found to be caused by a worn bearing in the actuator cross support (at point C in Figure 2.2). A jump in the strain measurements occurs every time the upper link changes direction. The jump is most clearly seen in the strain of the lower link when only the upper link is in motion, as is shown in Figure 4.6a, but is noticeable in every measurement. For example, Figure 4.5c shows a disturbance in the strain in the upper beam, at the same time that the disturbance occurs in the lower beam.

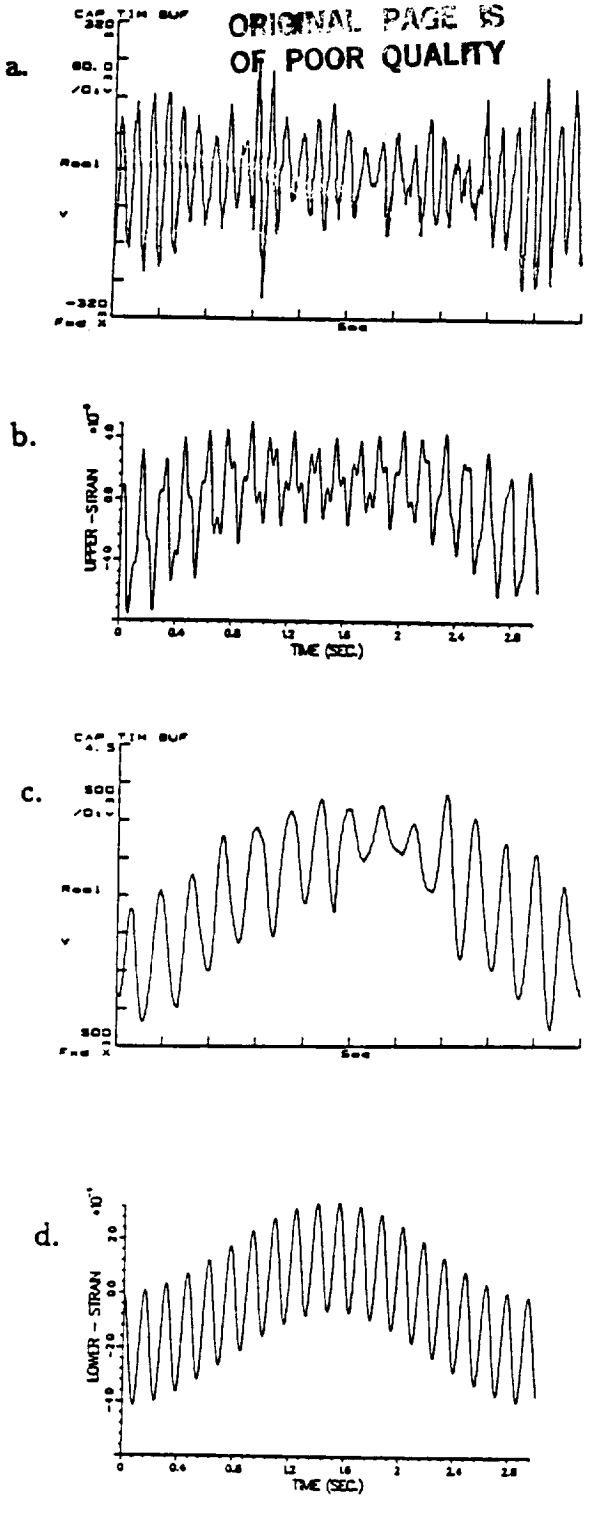

Figure 4.5
Strain of each link when both links moving
a. Measured strain in upper link
b. Simulated strain in upper link
c. Measured strain in lower link
d. Simulated strain in lower link

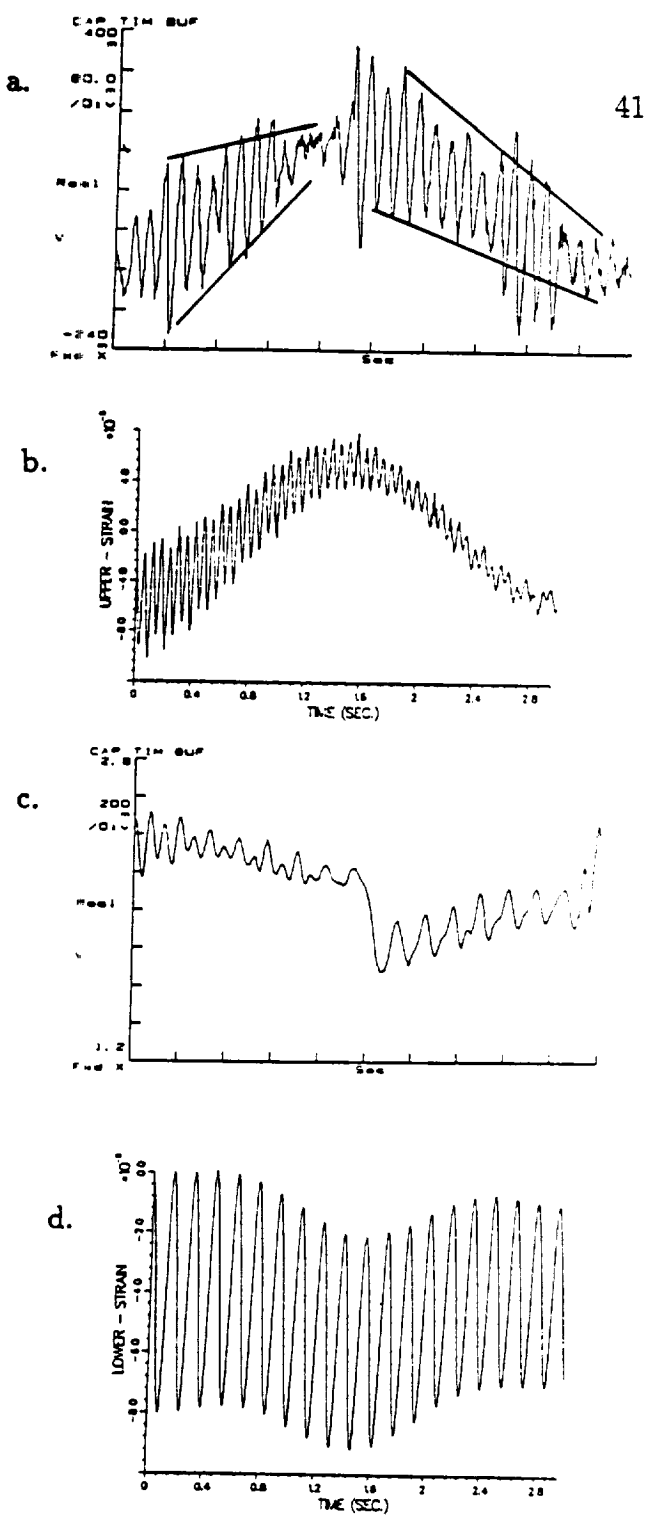

Figure 4.6
Strain of each link when only lower link moving
a. Measured strain in upper link
b. Simulated strain in upper link
c. Measured strain in lower link
d. Simulated strain in lower link

Comparison of Strain
Figures 4.5 and 4.6

Figure 4.6 shows the strain measurements in the upper and lower links when only the upper link is moving. The first discrepancy noticed is the jump in strain. Again, this was caused by the mechanical looseness in the actuator cross support. The similarity in the strain in the lower link, Figures 4.6a and 4.6b, is that both plots show little damping for the cycle of motion. Figure 4.6a shows more effect of the upper link's vibration than is predicted by the model, Figure 4.6b. Figures 4.6c and 4.6d show the strain in the upper beam. The measured strain in the upper beam clearly shows the effect of two disturbances. The first disturbance has already been discussed. The second disturbance, point A in Figure 4.6c, occurs at the maximum velocity and zero acceleration. A pure inertia load would display lost motion (backlash) at this point in the motion cycle. The reversal of differential pressure in the cylinder is another possible explanation for the observed disturbance. The seal deflection can result in behavior similar to backlash.

Figure 4.7 shows the control signal to second actuator, strain in the lower link, desired actuator position, and actual actuator position when only the upper joint is moving. The timing of the events is more obvious on this plot. Measurements of the differential pressure in the cylinder show that there is a 150 psi pressure variation concurrent with the disturbance. This may seem insignificant, but experience with the structure has shown that any disturbance seems large because of the large size of the structure and the use of large amplification of the strain signals. Figure 4.8 shows a plot of the differential pressure in the actuator when the input is a pure sine wave. As can be seen, there is a disturbance caused by a nonlinearity in the valve itself. The jump seen in the pressure measurements is clearly reflected in the measurement of strain on the links of the manipulator. Without the effect of these

two disturbances, the decrement of the amplitude of the strain in the experimental results would match fairly well with the decrement of the predicted strain as shown in Figure 4.6c and 4.6d (see the lines bounding the peaks).

It is obvious from these experiments that the experimental results do not exactly match the theoretical results. However, there is enough agreement in the general trend of the vibrations and their amplitudes when the disturbances are ignored to expect that the experimental results and the theoretical results can match if further efforts are made to reduce the disturbances in the experimental data.

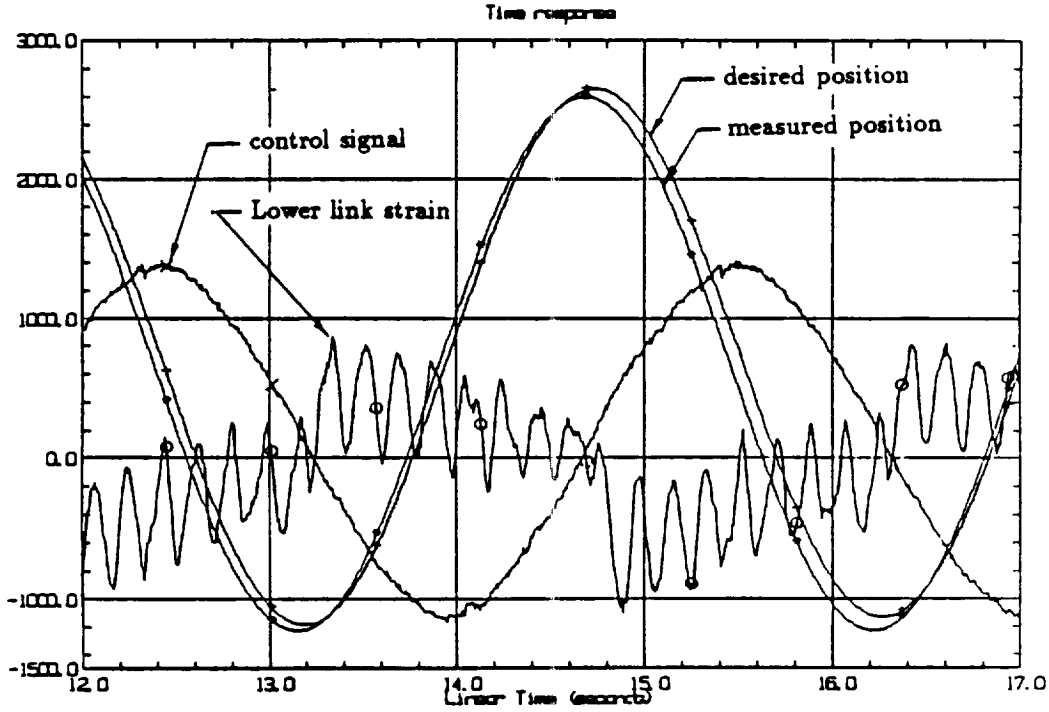

Control Signal, Strain, and Angle Position
Figure 4.7

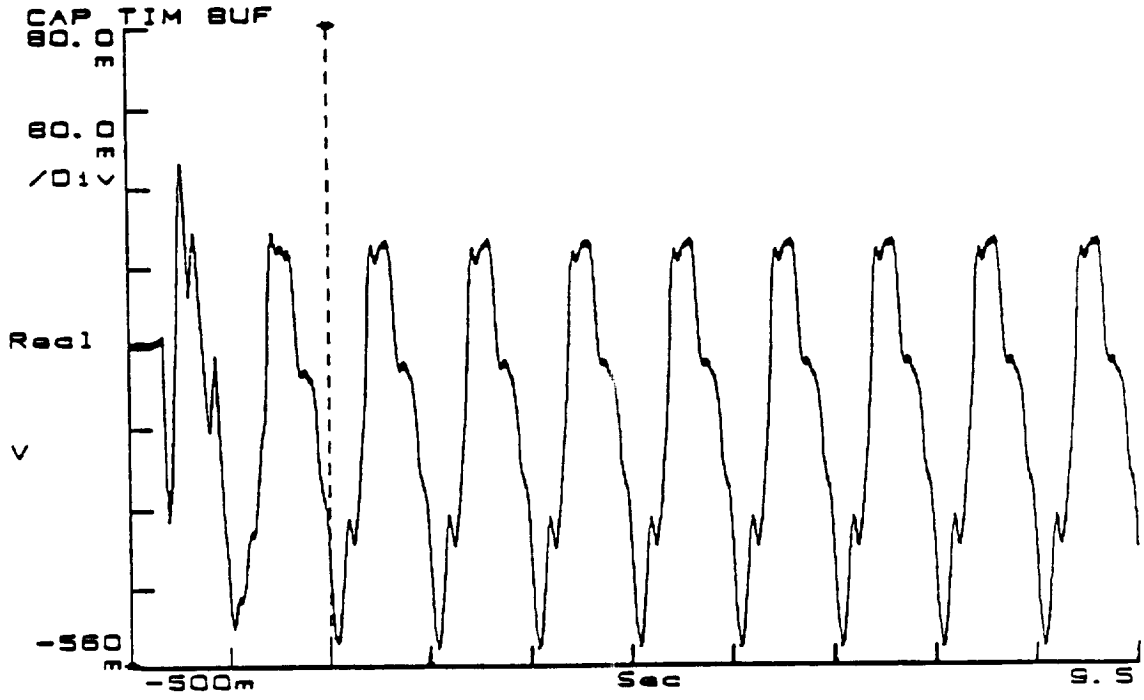

Differential Pressure in Actuator
Figure 4.8

CHAPTER V

Conclusions and Recommendations

The Lagrangian method for developing dynamics equations is very powerful. Simple flexible structures can use this method along with a finite number of modes to give accurate results. However, geometrically complicated structures, such as multilink manipulators and manipulators with parallel drive links, have very complicated constraint forces at the joints between the links so that simple boundary conditions can no longer be used. In addition, constraint forces, caused by redundant links used for strength considerations, change the mode shapes of the structure. These complications require that lightweight, flexible manipulators have experimental verification and subsequent modification of the system equations to provide accurate results.

As discussed in Chapter III, the eigenvalues and eigenvectors predicted by the linearized assumed modes modeling method are not exactly the same as those found by the FEM models and from experimental analysis. This was found to be primarily due to the simplifying assumptions used by the assumed modes model. This could be seen by noting the similarity between the system frequencies and modes shapes found with the simplified FEM model to the frequencies and modes shapes found using the assumed modes model. Then, as a more detailed FEM model was developed, the FEM model's results were seen to more nearly match the experimental results. From this, it can be concluded that the simplifying

assumptions used by the assumed modes model contribute heavily to the errors found in the system frequencies and modes shapes predicted by this modeling method. One solution to this is to use the FEM mode shapes or the experimentally determined mode shapes to adjust the parameters used in the assumed modes model.

In Chapter IV, the experimental results are seen to have a considerable amount of noise in them due to the imperfect structure and to jerks caused by the hydraulic actuators. The assumed modes model does not account for these disturbances so that their effect does not appear in the model's results. Another effect measured, but not predicted, is the flexibility of the manipulator between the actuator and the joint. The assumed modes model considers this section of the structure to be rigid and therefore does not model this behavior. Also, as discussed in Chapter IV, the limited workspace and the dominance of the first two system modes made it difficult to measure any nonlinear effects of the model. However, in spite of these imperfections in the experimental apparatus, the assumed modes model and the experimental results show very similar trends in the time domain measurements.

Recommendations

The assumed modes model can be improved by considering a more detailed geometry, however this will greatly increase the complexity of the equations. Better results can be obtained by incorporating the experimentally measured mode shapes or the FEM model's mode shapes. Better system frequency and mode shape determination may be determined experimentally by moving the shaker to several

locations on the manipulator or by using a multiple shaker techniques. Since the magnitude of the displacement of the 4^{th} and higher modes is on the order of 500 times smaller than the displacement of the first three modes, it may be that the model could be truncated after the 3^{rd} mode. This should be tested by adding the experimentally determined mode shapes to the assumed modes model, then comparing the new results to measured results. If more accuracy is required, the higher order modes can be added to the model.

For better measurement of the nonlinear aspects of the assumed modes model, position transducers capable of measuring the full range of actuator motion are needed. The speed of the data acquistion and digital controls implemented on the Microvax can be improved by using assembly level routines, but will require a considerably higher level of programming skill to implement. To reduce the noise caused by disturbances to the structure, more nearly ideal actuators or a more sophisticated control algorithm that incorporates an internal force loop around the hydraulic actuators themselves is needed. The joints of the manipulator could also be inproved by making the diameter of the pins larger and by making the joints stiffer, particularly in the out of plane direction. In addition, the base also should be enlarged and stiffened because small amounts of flexibility of the base could be seen easily in the experimental measurements. Finally, the manipulator's structure could be modified slightly to make it more ideal and more easily modeled so that specific aspects of the dynamic model could be more easily examined without the influence of unwanted disturbances.

APPENDICES

APPENDIX A

Derivation of Constrained Dynamic Equations

Constrained Equations of Motion

The following is excerpted from modeling done by Jae Won Lee. a Ph.D. candidate at Georgia Institute of Technology. This is the model used in verification of the manipulator.

To analyze a closed kinematic chain system, one joint of the flexible parallel link is virtually cut to form an open tree structure. An equation describing the constraint force at the point where the cut was made is then required. For this manipulator, the cut is made at the joint between the actuating link and the upper link. Lagrange's equations and the assumed mode method is used for deriving the equations of motion of this open tree flexible structure. In order to describe the motion, the reference frame is defined as shown in Figure A.1. The absolute position vectors of an arbitrary point on each link are described by the following:

$$\vec{r}_i = \vec{R}_i + \vec{U}_{ri} + \vec{U}_{fi} \qquad (A.2.1)$$

where $\vec{R}_i$ is the position vector of the origin of the reference body with respect to the global frame, $\vec{U}_{ri}$ is the undeformed position vector, and $\vec{U}_{fi}$ is the elastic deflection vector. $\vec{U}_{fi}$ is composed of a linear combination of an admissible shape

function, Ψ, multiplied by time dependant modal coordinates:

$$\vec{U}_{fi}(x,t) = \sum_{j=1}^{n} \Psi_{ij}(x) q_{f_{ij}}(t). \qquad (A.2.2)$$

Assuming that the amplitude of the higher modes of flexible links are much smaller than the amplitudes of the first two modes, the system can be truncated with n equal to 2.

The kinetic energy, T_i, of each element is obtained from the velocity vector of the infinitesimal volume:

$$T_i = \frac{1}{2}\rho \int \dot{\vec{r}}_i \cdot \dot{\vec{r}}_i dV. \qquad (A.2.3)$$

The strain energy, which is stored in the flexible mode, can be attributed to the elastic stiffness, K_i, which is evaluated by integration over the length of the beam:

$$K_i = (EI)_i \int_0^{l} \rho_{ij}''^2 dx \qquad (A.2.4)$$

The potential energy, V_i, of each element is composed of the strain energy and gravity force:

$$V_i = \frac{1}{2} q_{fi}^T K_i q_{fi} \qquad (A.2.5)$$

where E is Young's modulus of elasticity, and I is the area moment of inertia.

The governing dynamic equations for the system are derived through Lagrange's equations:

$$\frac{d}{dt}\left(\frac{\partial T}{\partial \dot{q}_j}\right) - \frac{dT}{dq_j} - \frac{dV}{dq} = Q_e \qquad (A.2.6)$$

The algebraic complexity in applying Lagrange's equation can be overcome using a symbolic manipulation program [41]. The open tree system is constrained by a set of nonlinear algebraic constraint equations. These constraint relations can be

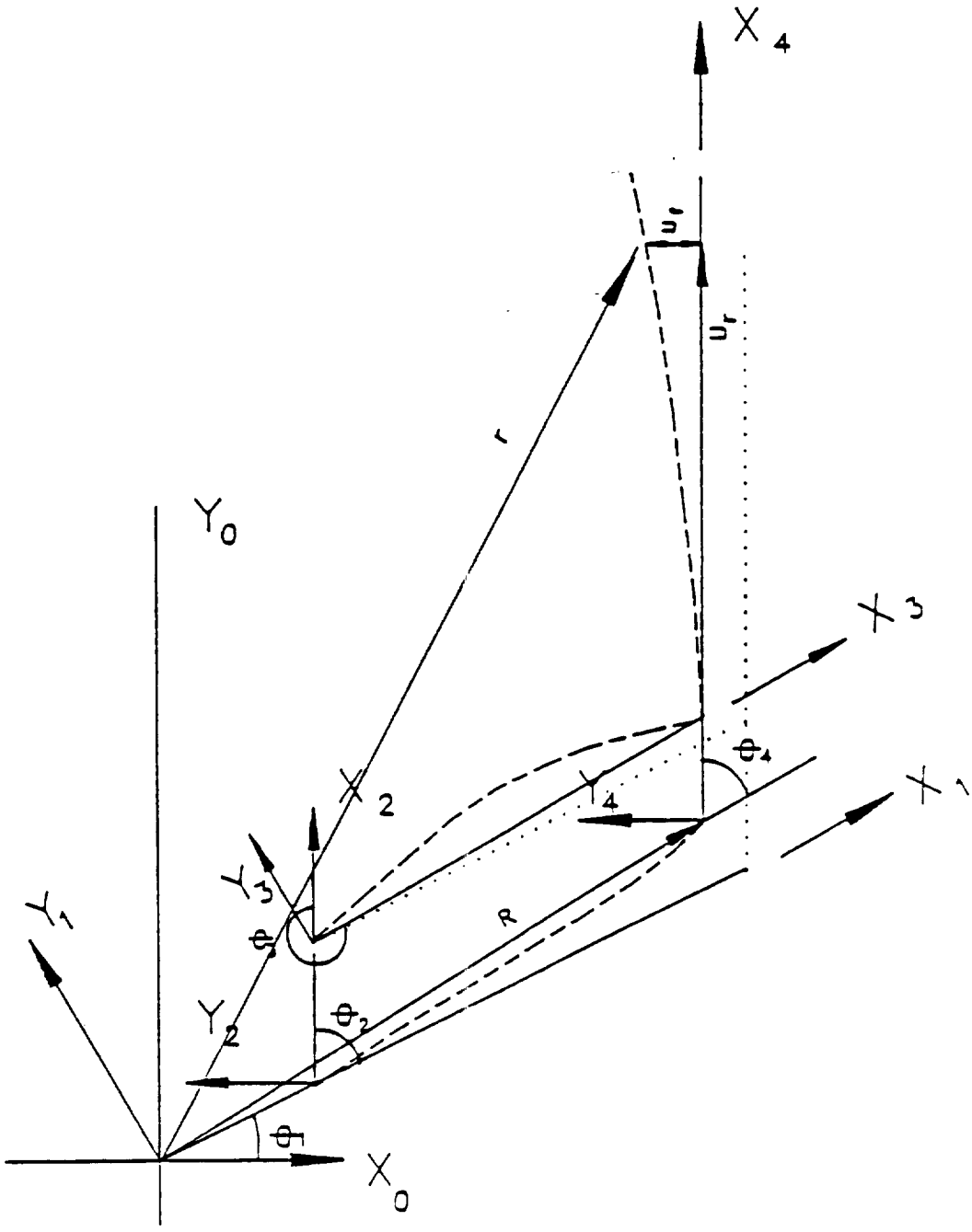

Coordinate Systems of Assumed Modes Model

Figure A.1

adjoined to equations (A.2.6) using Lagrangian multipliers. The resulting dynamic equations can be rewritten in partitioned form in terms of the rigid and flexible coordinates:

$$\begin{bmatrix} M_{rr} & M_{rf} \\ M_{fr} & M_{ff} \end{bmatrix} \begin{bmatrix} \ddot{q}_r \\ \ddot{q}_f \end{bmatrix} + \begin{bmatrix} 0 & 0 \\ 0 & K_{ff} \end{bmatrix} \lambda = \begin{bmatrix} Q_r \\ Q_f \end{bmatrix} \qquad (A.2.7)$$

where subscripts r and f denote rigid and flexible coordinates, q is the generalized coordinates vector, M is the generalized mass matrix, K is the elastic stiffness matrix, Φ_q is the constraint Jacobian matrix, λ is the unknown constraint force vector and Q is the generalized force vector including Coriolis, centrifugal and gravity forces. The m holonomic constraints are applied to the virtually cut joint as

$$\Phi(q) = 0 \qquad (A.2.8)$$

or

$$\Phi_q(q)\dot{q} = 0 \qquad (A.2.9)$$

where

$$\Phi_q = \frac{\partial \Phi}{\partial q} \qquad (A.2.10)$$

The initial conditions must be consistent with system constraints, therefore:

$$q(t_0) = q_0 \qquad (A.2.11.a)$$

and

$$\dot{q}(t_0) = \dot{q}_0 \qquad (A.2.11.b)$$

Singular Value Decomposition for Constrained Dynamic Analysis

The $m \times n$ constraint Jacobian matrix Φ_q with $m < n$ can be decomposed into the form

$$\Phi_q = U \Sigma V^T \tag{A.2.12}$$

or with proper partitioning [31]:

$$\Phi_q = [U_1 \quad U_2] [\Sigma_m \quad 0] \begin{bmatrix} V_1^T \\ V_2^T \end{bmatrix} \tag{A.2.13}$$

where U_i and V_i are orthonormal bases for four fundamental subspaces. The Σ_m is equal to $diag(\sigma_1, \sigma_2, \ldots, \sigma_m)$ where the σ_i's are called the singular values of matrix Φ_q, ordered $\sigma_1 > \sigma_2 > \ldots > 0$. The columns of U_i are the orthonormal eigenvectors of the symmetric matrix $\Phi_q^T \Phi_q$ with σ_i^2 the corresponding eigenvalues. The columns of V_i are the orthonormal eigenvectors of the symmetric matrix $\Phi_q \Phi_q^T$. It is noticeable that V_2 is the null space of Φ_q which satisfies the following relation:

$$\Phi_q V_2 = 0 \tag{A.2.14}$$

and Φ_q^+, called the pseudo inverse of Φ_q , is defined as

$$\Phi_q^+ = [V_1 \quad V_2] \begin{bmatrix} \Sigma_m^{-1} \\ 0 \end{bmatrix} \begin{bmatrix} U_1^T \\ U_2^T \end{bmatrix} \tag{A.2.15}$$

Using the nullity of $\Phi_q V_2$, an algorithm which eliminates the constraint forces from the equations of motion can be developed. Premultiplication by V_2^T in equation (A.2.7) gives

$$V_2^T M \ddot{q} + V_2^T K q = V_2^T Q \tag{A.2.16}$$

since $\Phi_q V_2 = 0$. Because the dimension of equation (A.2.16) is $(n - m) \times n$, an additional equation is needed to get the solution. A new variable, z, is defined

which is a constrained independent coordinate with dimension $n - m$. Then $V_2\dot{z}$ is the homogeneous solution to equation (A.2.9). That is,

$$\dot{q} = V_2\dot{z}. \tag{A.2.17}$$

Geometrically, equation (A.2.17) is the projection of the velocity vector, q, onto the tangent hyperplane of the constraint surface. Similarly, the time derivative of equation (A.2.9) gives

$$\Phi_q\ddot{q} = -(\Phi_q)_q\dot{q}^2. \tag{A.2.18}$$

Due to the nullspace of Φ_q, $V_2\ddot{z}$ is also the homogeneous solution to equation (A.2.18). Then $\ddot{q}$ can be written as

$$\ddot{q} = -\Phi_q^+(\Phi_q)_q\dot{q}^2 + V_2\ddot{z} \tag{A.2.19}$$

Physically, the first and second terms on the right hand side of equation (A.2.19) represent the normal and tangential accelerations, respectively. By integrating equation (A.2.17), q is expressed as

$$q = V_2 z + C \tag{A.2.20}$$

where the constant C is chosen as zero to satisfy the constraint equation. Hence, the following $n - m$ independent equations can be derived from equations (A.2.16), (A.2.17) and (A.2.19):

$$V_2^T M V_2\ddot{z} + V_2^T K V_2 z = V_2^T Q + V_2^T M\Phi_q^+(\Phi_q)_q(V_2\dot{z})^2 \tag{A.2.21}$$

where q and $\dot{q}$ are calculated using equations (A.2.20) and (A.2.17). These are the equations used for the nonlinear dynamic simulation.

Natural Frequencies and Mode Shapes

The eigenvalues (natural frequencies) and eigenvectors (mode shapes) are obtained from the equations of motion of the reduced equations (A.2.21) linearized about zero velocity.

$$V_2^T M V_2 \ddot{z} + V_2^T K V_2 z = 0 \tag{A.3.1}$$

Eigenvalues of (A.3.1) are the same as those of the constrained equation (A.2.7). Eigenvectors of the constrained system are derived by transforming those of (A.3.1) as

$$q = V_2 z. \tag{A.3.2}$$

For numerical analysis, the selection of mode shape functions is necessary and may greatly influence the results. Clamped-mass boundary conditions are assumed for the lower link mode shape. Clamped-free boundary conditions are used for the upper link. Pin-pin boundary conditions are used for the actuating link. In previous work [10], the natural frequencies were derived by the flexible part of the unconstrained equations:

$$M_{ff}\ddot{q} + K_{ff} q = 0 \tag{A.3.3}$$

but more accurate results were obtained by considering that the lower link bending is affected by the actuating link's rigid motion. The constrained dynamics including the actuator link motion is then needed. When the actuators are fixed, velocities of joint 1 and joint 2 are zero. New constraint equations between joint 3, joint 4 and the elastic coordinates are needed. The elements of the mass matrix related to joint 1 and joint 2 (columns 1 and 2; rows 1 and 2) are deleted. The dynamic equation can then be rewritten as

$$\bar{V}_2^T \bar{M} \bar{V}_2 \ddot{Z} + \bar{V}_2^T \bar{K} \bar{V}_2 Z = 0. \tag{A.3.4}$$

From these equations, the natural frequencies are calculated and the eigenvectors are obtained by the transformation, $q = V_2 Z$.

APPENDIX B

Derivation of A General Two Link Manipulator

The task of solving the forward and inverse kinematics of a general two link manipulator can be thought of as relating the endpoint of the manipulator to the fixed coordinate system having its origin at the axis of the first joint. This derivation assumes that both the links are rigid members. Figure B.1 illustrates the coordinate system used for this derivation.

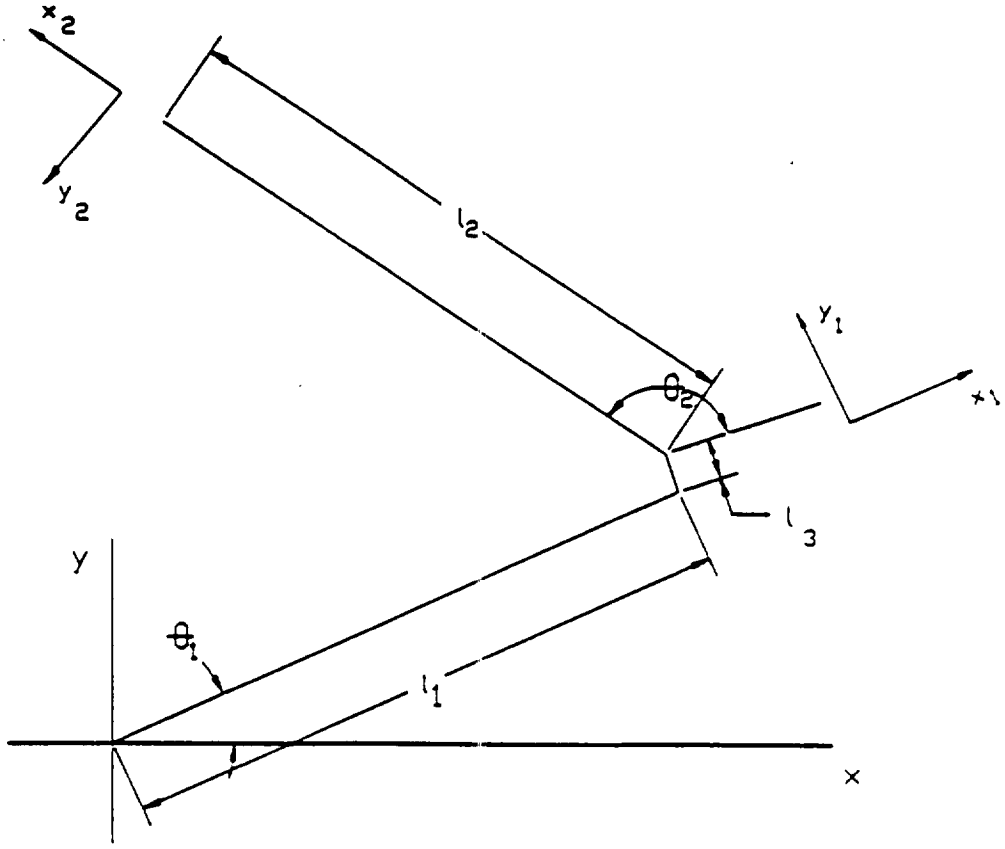

Two Link Rigid Body Coordinate System
Figure B.1

The following variables are used throughout.

$l_1 = length\ of\ the\ first\ link$

$l_2 = length\ of\ the\ second\ link$

$l_3 = offset\ between\ the\ first\ link\ axis\ and\ the\ second\ joint\ axis$

$C_1 = cosine\ \theta_1$

$C_2 = sine\ \theta_2$

$S_1 = cosine\ \theta_1$

$S_2 = sine\ \theta_2$

This coordinate transformation is represented by a series of rotations and translations in matrix form. These are multiplied together to obtain the total transformation for the endpoint. Both the forward and inverse kinematics can be found from the total transformation matrix.

To move a point from the origin to the end of the first link, the following two transformations are used.

$$T_1 = \begin{bmatrix} C_1 & S_1 & 0 & 0 \\ -S_1 & C_1 & 0 & 0 \\ 0 & 0 & 1 & 0 \\ 0 & 0 & 0 & 1 \end{bmatrix} \begin{bmatrix} 1 & 0 & 0 & l_1 \\ 0 & 1 & 0 & l_3 \\ 0 & 0 & 1 & 0 \\ 0 & 0 & 0 & 1 \end{bmatrix}$$

$$T_1 = \begin{bmatrix} C_1 & S_1 & 0 & (l_1 C_1 + l_3 S_1) \\ -S_1 & C_1 & 0 & (-l_1 S_1 + l_3 C_1) \\ 0 & 0 & 1 & 0 \\ 0 & 0 & 0 & 1 \end{bmatrix}$$

To move from the end of the first link to the end of the second link another rotation and translation is made.

$$T_2 = \begin{bmatrix} C_2 & S_2 & 0 & 0 \\ -S_2 & C_2 & 0 & 0 \\ 0 & 0 & 1 & 0 \\ 0 & 0 & 0 & 1 \end{bmatrix} \begin{bmatrix} 1 & 0 & 0 & l_2 \\ 0 & 1 & 0 & 0 \\ 0 & 0 & 1 & 0 \\ 0 & 0 & 0 & 1 \end{bmatrix}$$

$$T_2 = \begin{bmatrix} C_2 & S_2 & 0 & l_2C_2 \\ -S_2 & C_2 & 0 & -l_2S_2 \\ 0 & 0 & 1 & 0 \\ 0 & 0 & 0 & 1 \end{bmatrix}$$

The total transformation matrix is the product of T_1 and T_2.

$$T_1T_2 = \begin{bmatrix} \alpha_{11} & \alpha_{12} & \alpha_{13} & \alpha_{14} \\ \alpha_{21} & \alpha_{22} & \alpha_{23} & \alpha_{24} \\ \alpha_{31} & \alpha_{32} & \alpha_{33} & \alpha_{34} \\ \alpha_{41} & \alpha_{42} & \alpha_{43} & \alpha_{44} \end{bmatrix}$$

where

$$\alpha_{11} = C_1C_2 - S_1S_2$$

$$\alpha_{12} = C_1S_2 + S_1C_2$$

$$\alpha_{13} = 0$$

$$\alpha_{14} = l_2(C_1C_2 - S_1S_2) + l_1C_1 + l_3S_1$$

$$\alpha_{21} = -(S_1C_2 + C_1S_2)$$

$$\alpha_{22} = C_1C_2 - S_1S_2$$

$$\alpha_{23} = 0$$

$$\alpha_{24} = -l_2(S_1C_2 + C_1S_2) - l_1S_1 + l_3C_1$$

$$\alpha_{31} = 0$$

$$\alpha_{32} = 0$$

$$\alpha_{33} = 1$$

$$\alpha_{34} = 0$$

$$\alpha_{41} = 0$$

$$\alpha_{42} = 0$$

$$\alpha_{43} = 0$$

$$\alpha_{44} = 1$$

The fourth column of the resultant matrix is the displacement vector. Since the forward kinematic solution assumes that θ_1 and θ_2 are known, the X and Y positions can be found from the following equations:

$$X = l_2(C_1C_2 - S_1S_2) + l_1C_1 + l_3S_1 \qquad (B.1)$$

$$Y = -l_2(S_1C_2 + C_1S_2) - l_1S_1 + l_3C_1 \qquad (B.2)$$

or using a trigonometric identity,

$$X = l_2(\cos(\theta_1 + \theta_2)) + l_1C_1 + l_3S_1 \qquad (B.3)$$

$$Y = -l_2(\sin(\theta_1 + \theta_2)) - l_1S_1 + l_3C_1 \qquad (B.4)$$

It should be noted that θ_2 is measured relative to the axis of the second link.

To find the inverse kinematic solution square equations (B.3) and (B.4), then add the results together to obtain:

$$X^2 + Y^2 = l_1^2 + l_2^2 + l_3^2 + 2l_1l_2C_2 - 2l_2l_3S_2$$

$$\text{Let } K = X^2 + Y^2 - l_1^2 - l_2^2 - l_3^2$$

$$K = 2l_1l_2C_2 - 2l_2l_3S_2$$

Solve for C_2:

$$C_2 = \frac{K + 2l_2l_3S_2}{2l_1l_2}$$

From the trigonometric identity:

$$S_2 = \sqrt{1 - C_2^2}$$

Substituting for S_2 and squaring both sides of the equation yields:

$$C_2^2 = \frac{K^2 + 4Kl_2l_3S_2 + 4l_2^2l_3^2S_2^2}{4l_1^2l_2^2}$$

Then substitute for C_2^2 to get:

$$S_2^2 = \frac{4l_1^2l_2^2 - 4Kl_2l_3S_2 - 4l_2^2l_3^2S_2^2 - K^2}{4l_1^2l_2^2}$$

or

$$S_2 = \frac{-Kl_3 \pm \sqrt{4(l_1^4l_2^2 + l_1^2l_2^2l_3^2) - K^2l_1^2}}{2l_2(l_1^2 + l_3^2)}. \qquad (B.5)$$

Due to the direction of the offset l_3 the root of equation (B.5) that is associated with the minus sign is the proper solution, so that:

$$S_2 = \frac{-Kl_3 - \sqrt{4(l_1^4l_2^2 + l_1^2l_2^2l_3^2) - K^2l_1^2}}{2l_2(l_1^2 + l_3^2)} \qquad (B.5a)$$

$$C_2 = \frac{Kl_1 - l_3\sqrt{4(l_1^2l_2^2 + l_2^2l_3^2) - K^2}}{2l_2(l_1^2 + l_3^2)} \qquad (B.6)$$

$$\tan\theta_2 = \frac{S_2}{C_2} = \frac{-Kl_3 - \sqrt{4(l_1^4l_2^2 + l_1^2l_2^2l_3^2) - K^2l_1^2}}{Kl_1 - l_3\sqrt{4(l_1^2l_2^2 + l_2^2l_3^2) - K^2}} \qquad (B.7)$$

Since all of the lengths of the robot arm are known quantities, θ_2 can be found by taking the arctangent of the right hand side of equation (B.7). To solve for θ_1, equations (B.1) and (B.2) are rearranged as follows:

$$X = C_1(C_2l_2 + l_1) + S_1(l_3 - l_2S_2)$$

$$Y = C_1(l_3 - l_2S_2) + S_1(-l_2C_2 - l_1)$$

Putting these equations into matrix form yields:

$$\begin{bmatrix} X \\ Y \end{bmatrix} = \begin{bmatrix} C_2l_2 + l_1 & l_3 - l_2S_2 \\ l_3 - l_2S_2 & -l_2C_2 - l_1 \end{bmatrix}$$

Using Cramer's rule to solve for $\cos\theta_1$ and $\sin\theta_1$:

$$\cos\theta_1 = \frac{-X(l_2C_2 + l_1) - Y(l_3 - l_2S_2)}{-l_1^2 - (C_2l_2)^2 - 2l_1l_2C_2 - (l_3 - l_2S_2)^2} \qquad (B.8)$$

$$\sin\theta_1 = \frac{Y(C_2l_2 + l_1) - X(l_3 - l_2S_2)}{-l_1^2 - (C_2l_2)^2 - 2l_1l_2C_2 - (l_3 - l_2S_2)^2} \qquad (B.9)$$

$$\tan\theta_1 = \frac{S_1}{C_1} = \frac{Y(C_2l_2 + l_1) - X(l_3 - l_2S_2)}{-X(l_2C_2 + l_1) - Y(l_3 - l_2S_2)} \qquad (B.10)$$

Since all the quantities on the right hand side of equation (10) are known, θ_1 can be found using the arctangent function.

APPENDIX C

Equipment List

COMPUTER EQUIPMENT

Model:	Microvax II (VS21W-A2)
Serial No.	WF 61305804
Company:	Digital Equipment Co. Boston, MA

Additional Boards for Microvax

Model:	DT2769–Real Time Clock Board
Model:	DT2785–Analog I/O System (2) 8 channels A/D multiplexed 2 channels D/A 12 bit resolution
Company:	Data Translation Canterbury, MA

Software for Microvax

	IDEAS Geomod Supertab Tdas
Company:	Structural Dynamics Research Corp. Cincinnati, OH

Signal Analyzers

Model:	3562A–Digital Signal Analyzer
Serial No.:	2502A00718
Model:	9122–Disk Storage Unit
Serial No.:	2518A44227
Company:	Hewlett-Packard Co. San Jose, CA

SENSORS

Model:	604-000 Angle Transducer (2)
Serial Nos.:	L-6, L-7
Resolution:	infinite
Range:	60 degrees
Company:	Transtek, Inc. Ellington, Connecticut

Part No.:	B1105H3311 Tachometers (with Hall Sensors) (2)
Serial Nos.:	875308, 875309
Output:	2.6 Volts per 1000 rpm
Company:	Harowe Servo Controls, Inc. Pennsylvania
Model:	308B Accelerometer
Serial No.:	10430
Model:	208A04 Force Transducer
Serial No.:	5978
Model:	480D06 Power Unit (2)
Serial Nos.:	5163, 5164
Company:	PCB Piezotronics, Inc. Depew, NY
Model:	4375 Accelerometer
Serial No.:	886208
Model:	2635 Charge Amplifier
Serial No.:	900977
Model:	2651 Charge Amplifier
Serial No.:	488592
Company:	Bruel & Kjaer Instruments, Inc. Marlboro, MA
Model:	EA-13-250MQ-350 Strain Gages
Company:	Measurements Group, Inc. Micro-Measurements Div. Raleigh, NC

The graphs at the end of this appendix show the static calibration of the strain gages mounted on the lower and upper links, respectively.

HYDRAULIC COMPONENTS

Power Unit

	Delco Electric Motor
Size:	25 hp., 230 volts, 60.8 amps, 1755 rpm
Pump:	Vickers Variable Volume Piston Pump - 20 gpm
Model:	F3-PVB20-FRS-20-C-11
Company:	Parker Hannifin Corp. Aurora, NY

Valves

Model:	73-102A Two Stage Servovalves - 5 gpm (2)
Serial Nos.:	147, 153
Company:	Moog, Inc. East Aurora, NY

Cylinders

Model:	N2C - 3.25 x 40 Cylinder
Serial No.:	5C8205-065-1B

Bore:	3.25 in.
Stroke:	40 in. (modified to 17 in.)
Seals:	Buna-N
Rod Diameter:	1.75 in.
Piston Diameter:	3.25 in.
Weight:	52 lbs.
Company:	Hydroline Mfg. Co. Rockford, IL

Model:	H-PB-2 Cylinder
Serial No.:	37781-J
Bore:	2 in.
Stroke:	20 in.
Seals:	Teflon
Rod Diameter:	1.00 in.
Weight:	35 lbs.
Company:	Atlas Cylinder Corp. Eugene, OR

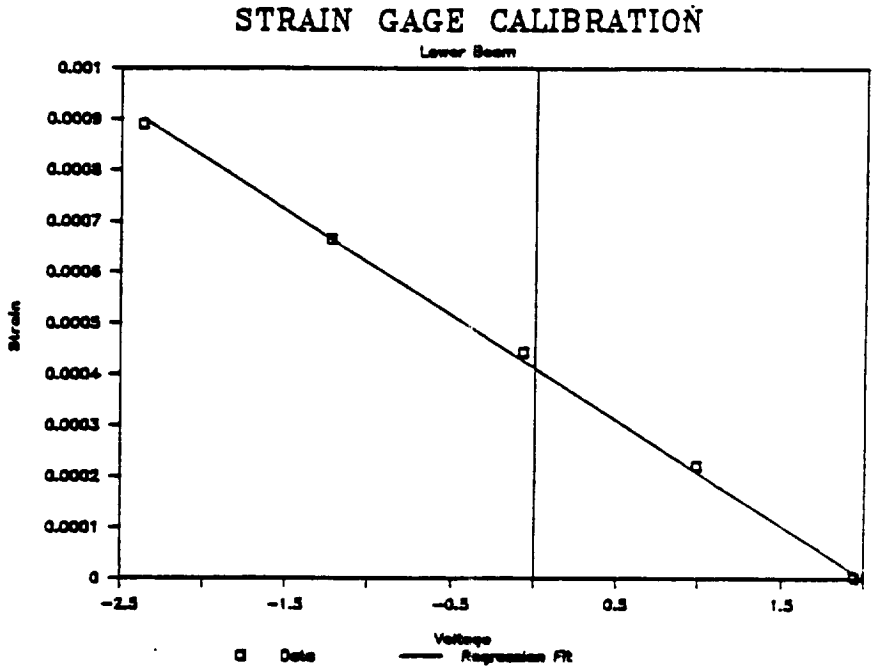

Strain Gage Calibration, Lower Beam
Figure C.1

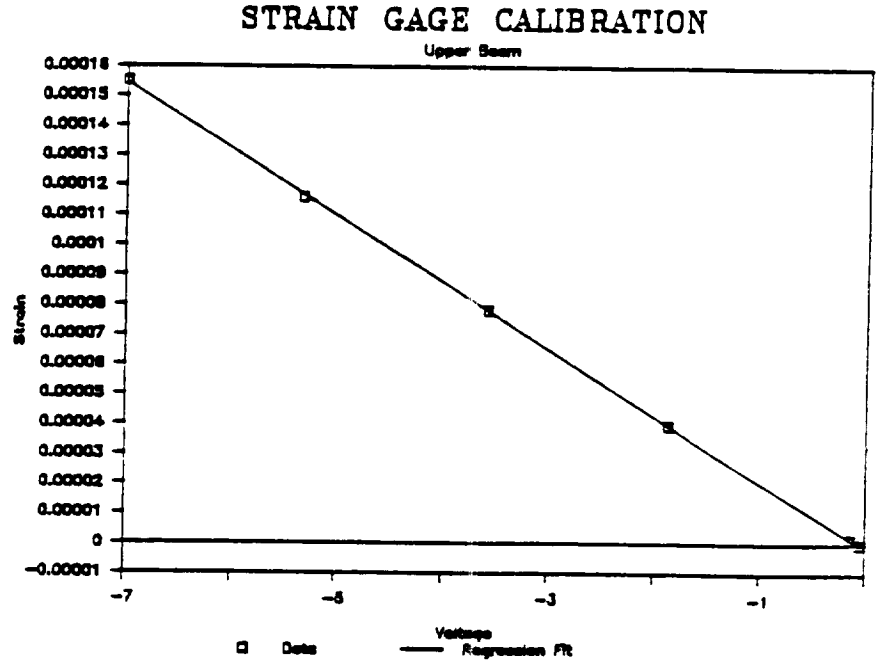

Strain Gage Calibration, Upper Beam
Figure C.2

APPENDIX D

Computer Programs

For verifying the nonlinear aspects of the assumed modes model, it was important to be able to move the manipulator in a controlled manner along a given path and to be able to gather DATA about that movement at the same time. It was decided to implement control and data acquisition on a Digital Equipment Co. Microvax II to which A/D and D/A capability had been added. Along with the A/D board came compiled software routines that could be called from Fortran or C programs. In this work, all programs were written in Fortran.

Two types of programs were written. The first type was a program to gather data only. This was used to verify the system mode shapes and system frequencies. The second type of program included path planning for the manipulator, control of the movements, and data acquisition. Both programs include the ability to write the data to a standard file format. The programs are similar in that they both use the Data Translation supplied subroutines to initialize the A/D board and to capture the data. The sequence for initializing the A/D boards is as follows:

1. Include the MicroVms Library at the start of the Fortran program.

2. Assign a logical name to the A/D board and to the Real Time Clock board.

3. Call the subroutine DTDEV for each device used, supplying in the CALL

argument the logical name of the device.

4. Set up the A/D board for the number of channels to be used by calling either DTALCH, DT1CH, or DTISCN.

5. Set the gain for all channels by calling DTADGN.

6. Set up the timing of the Real Time Clock board by calling DTCLOK and supplying the appropriate parameters.

7. Define an array (buffer) that will accept the data by calling the subroutine DTSBDB.

After this, the computer is ready to read in data. The above steps only have to be done once for each program. The data is read into the buffer using the subroutines DTSBR and DTSBWB. DTSBR reads the A/D channels. DTSBWB causes the computer to wait until the buffer is full before proceeding. More details about these subroutines can be found in the Data Translation manual [43]. After initialization, the DTSBR and DTSBWB routines can be called repeatedly to transfer the data. It should be noted that these are referred to in the Data Translation manuals as single buffer routines. The manual implies that the multibuffer routines are faster. In this case, however, the multibuffer is really only a large single buffer that has been partitioned. No increase in speed is seen except the routines don't have to be called repeatedly to gather the same data. Since the control algorithms require a sample then time to compute the control effort, the multiple buffer routines were judged unsuitable in this case. A single buffer of 8 was used in programs for controlling the manipulator. A single buffer of 10,000 was

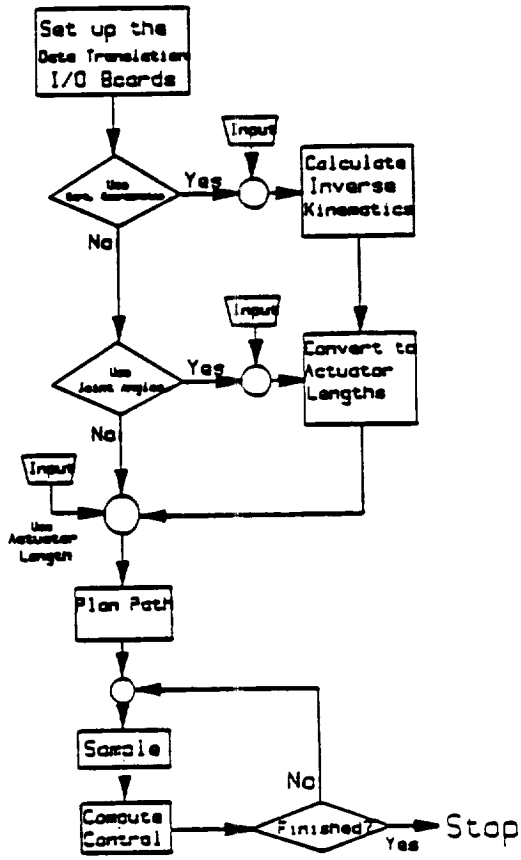

Computer Flow Diagram
Figure D.1

used for programs that gathered data only.

Figure D.1 shows a simple flow diagram of the computer program used for control and data acquisition. After the A/D board has been initialized, the user is prompted for the options for planning the manipulator's path. The choices are to plan the path in joint space, in cartesian space, or in terms of the actuator's position. If either the joint space or cartesian space option is chosen, the computer calculates the desired path with the options chosen then solves the inverse kinematics to find the desired actuator positions at each point along the path.

The equations used for this are outlined in Appendix B. If the actuator option is chosen, the path is computed directly from the values input from the keyboard. In all option cases, the user is prompted for the speed that he wishes to move the manipulator along the path. Note that two paths were programmed for these tests. The first path is from work done by Oosting [44]. The second is a pure sine wave.

As the path was computed, the desired actuator displacements were stored in an array. The array's size varies according to the requested speed of the manipulator (More values for slower movements, less values for fast movements). Since the D/A board has no provision for timing the analog output, the speed of the A/D input had to be used to control the speed of the output. The input/compute cycle time length was measured and then included in the path planning algorithm. This is inconvenient because as the control algorithm is modified, the time factor also may change causing inaccuracies. After all the above steps, the manipulator is ready for movement.

To make a movement, the transducers are sampled, the control is computed, and an analog value is output to the power amplifiers that is proportional to the error between the planned path's actuator displacements and the measured actuator position. This is repeated until the planned path is completed. The manipulator position is maintained until a key is pressed on the keyboard. The user is then prompted for another move or to stop the controller. A listing of the computer programs is included in a separate report, "User's Guide to Flexible Manipulator Control on the Microvax." The program listings are too long to include in this thesis. A more detailed discussion of the control used follows in Appendix E.

APPENDIX E

Manipulator Control

The controller used for the manipulator is a simple PI controller. This was implemented digitally using a zero order hold conversion from the analog equivalent. What follows is a discussion of the gains used and the conversions resulting from the characteristics of the particular equipment used. Figure E.1 shows the simplified block diagram of the controller. Figures E.2 through E.4 show more detail of the blocks in Figure E.1.

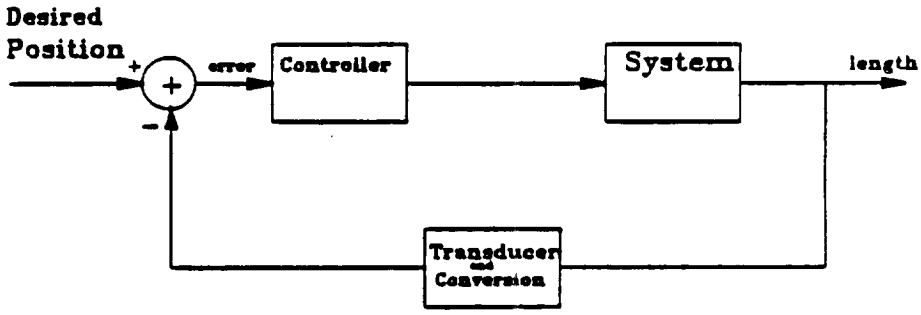

Overall Block Diagram
Figure E.1

Because the computer deals only with numbers, the voltages from the transducers must be converted to numbers via the A/D converter. These numbers

were then multiplied times a gain and an offset was added to obtain another number that represents a physical quantity on the manipulator, the length of the actuator.

The planned path is a series of numbers representing the desired actuator displacement in inches of length. Therefore, to accurately compare the desired position with the measured position, the transducer measuring the actuator's position had to be converted to inches of actuator position. Assuming the output of the transducer is linear, the equation that represents this is:

$$y = mx + b$$

where y is the actuator position, x is the transducer voltage, m is the transducer gain, and b is an offset. Each time the transducer is mounted, it must be calibrated and the computer program modified accordingly. Also each transducer has a different gain so that each must be tested to give accurate results. In the computer routines used, the subroutine used for performing this calculation is called HOMEPOS. A block diagram of this is in Figure E.2.

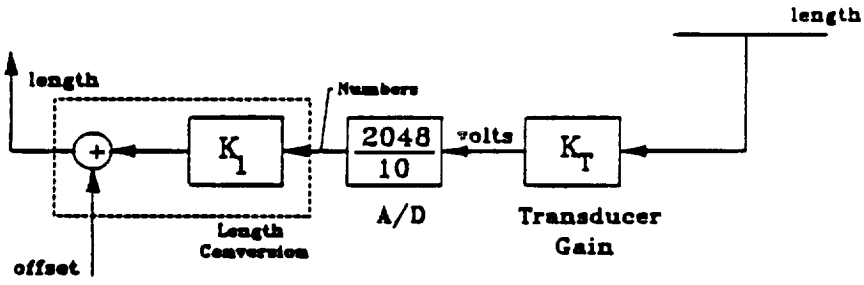

Block Diagram of Transducer
Figure E.2

The error between the desired position and the measured position is multiplied by a gain, K_c. This gain is the only value in the control loop that is selectable by the user. The computer program prompts the user for the gain. Typical values used were 3000 and 9000 for Joint 1 and Joint 1, respectively. These values were used to match the digital controller's gains to those found from frequency response tests made with the analog controller. The controller block, then, is very simple, as shown in Figure E.3.

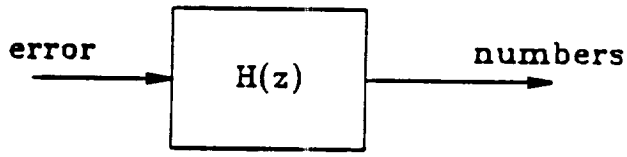

Block Diagram of Controller
Figure E.3

where H(z) is:

$$\frac{K_c(z - .9993)}{z - 1.}$$

Notice that the output of the controller is a number proportional to the error. The block diagram of the system is examined next. Figure E.4 shows the block diagram of the system.

These are the fixed conversions of the physical components in the apparatus. The overall gain for the system subblock is:

$$\frac{10}{2048}\frac{.020}{10}\frac{5}{.020}\frac{231}{60}\frac{1}{Area} = \frac{.0094}{Area}$$

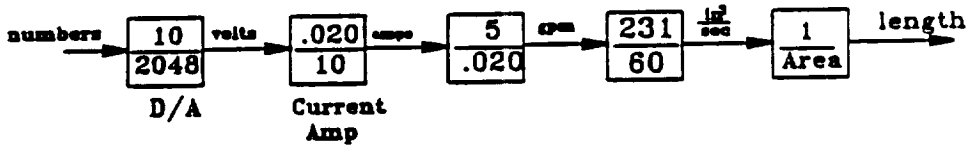

Block Diagram of the System
Figure E.4

The units of the system gain are $\frac{(in/sec)}{numbers}$. The low magnitude of the system numerator is the reason for the high gains required by the digital controller.

Hydraulic Actuators

The following the Bode plots show the open loop response and closed loop response of the hydraulic actuators when detached from the manipulator. From these the open loop gains and the closed loop phase and gain margins were determined.

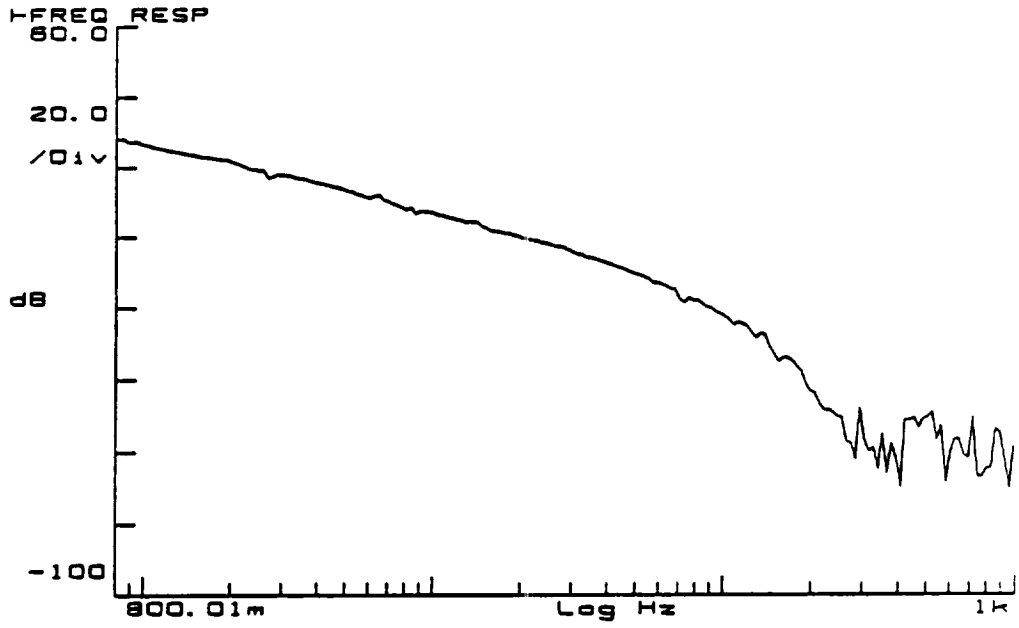

Open Loop Response of Joint 1
Figure E.5

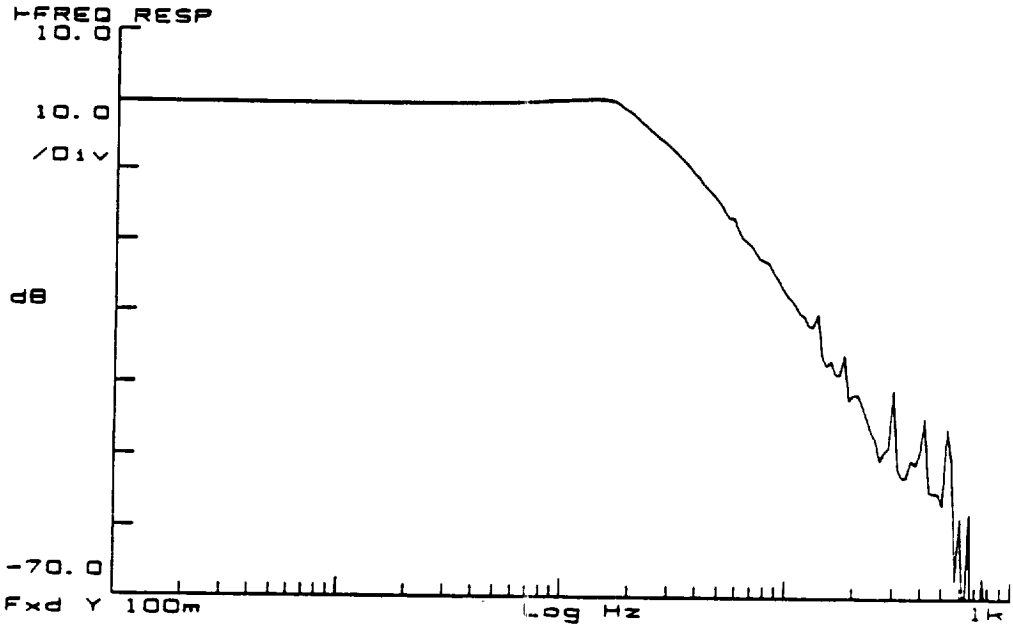

Closed Loop Response of Joint 1
Figure E.6

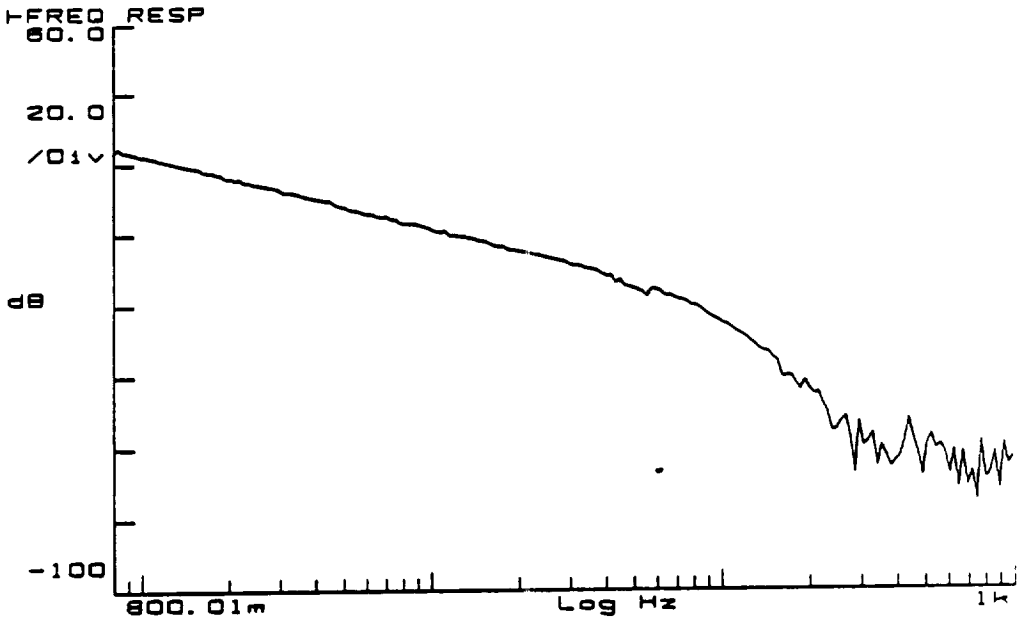

Open Loop Response of Joint 2
Figure E.7

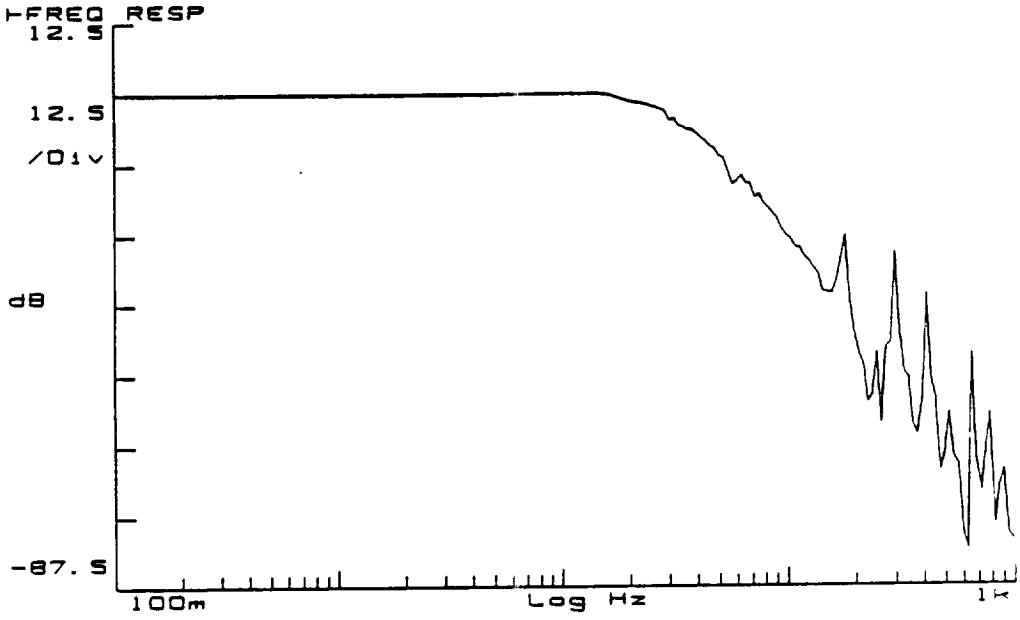

Closed Loop Response of Joint 2
Figure E.8

BIBLIOGRAPHY

[1] Wilson, Thomas R., "The Design and Construction of a Flexible Manipulator," Master's Thesis, School of Mechanical Engineering, Georgia Institute of Technology, March 1986.

[2] Hastings, G. G., "Controlling Flexible Manipulators, An Experimental Investigation," Ph.D Thesis, School of Mechanical Engineering, Georgia Institute of Technology, August, 1986.

[3] Schmitz, E., "Experiments on the End-Point Position Control of a Very Flexible One Link Manipulator," Ph.D. Thesis, Department of Aeronautics and Astronautics, Stanford University, June, 1985.

[4] Kanoh, H., and Lee, H.G., "Vibration Control of One Link Flexible Arm," *Proc. of* 24^{th} *IEEE Conf. on Decision and Control*, 3, Dec. 1985.

[5] Sakawa, Y., Masuno, F., and Fukushima, S., "Modeling and Feedback Control of a Flexible Arm," *Journal of Robotic Systems*, 2(4), 1985, pp. 453-472.

[6] Book, W.J., "Analysis of Massless Elastic Chains with Servo Controlled Joints," *ASME Journal of Dynamic Systems, Measurement, and Control*, 101, Sept. 1979, pp. 187-192.

[7] Book, W.J., "Recursive Lagrangian Dynamics of Flexible Manipulator Arms," *The Int'l Journal of Robotics Research*, Fall 1984, pp. 87-101.

[8] Book, W.J., "Modeling, Design, and Control of Flexible Manipulator Arms," Ph.D. Thesis, Dept. of Mechanical Engineering, Massachusetts Institute of Technology, April 1974.

[9] Maizza-Neto, O., "Modal Analysis and Control of Flexible Manipulator Arms," Ph.D. Thesis, Dept. of Mechanical Engineering, Massachusetts Institute of Technology, Sept. 1974.

[10] Huggins, J.D., Kwon, D.S., Lee, J.W., and Book, W.J., "Alternative Modeling and Verification Techniques for a Large Flexible Arm," *Applied Motion Control Conference*, June 1987, pp. 157-164.

[11] Fukada, T., and Kuribayashi, Y., "Flexibility Control of Elasic Robot Arms and Its Application to Contouring Control,"

[12] Asada, H., Ma, Z.D., and Tokumaru, H., "Inverse Dynamics of Flexible Robot Arms for Trajectory Control," ASME, Winter Annual Meeting, 1987.

[13] Mirro, J., "Automatic Feedback Control of a Vibrating Beam," Master's Thesis, Dept. of Mechanical Engineering, Massachusetts Institute of Technology, Rept. T-571, Cambridge, MA, C.S. Draper Lab., 1972.

[14] Fukada, T. "Control of a Flexible Robot Arm," *Bulletin of Japanese Society of ME*, Vol. 29, #250, 1986, pp. 1269-1273.

[15] Matsuno, F., Fukushima, S., Ohsawa, Y., Kiyohara, M., and Sakawa, Y., "Feedback Control of a Flexible Manipulator with a Parallel Drive Mechanism,"

[16] Truckenbrodt, A. "Modeling and Control of Flexible Manipulator Structures," 4^{th} *CISM-IFTOMM Symp. on Theory and Practice of Robots and Manipulators* pp. 90-101.

[17] Gebler, B., "Feed-Forward Control Strategy for an Industrial Robot with Elastic Links and Joints," *IEEE*, Ch2413 -3 / 87 / 0, 1987!

[18] Henrichfreise, H., Moritz, W., and Siemensmeyer, H., "Control of a Light, Elastic Manipulation Device," *Conference on Applied Motion Control*, June 1987, pp.

[19] Priebe, J., Hennessey, M., Johnson, B., Huang, P., and Grommes, R., "Design and Control of a Lightweight Robotic Arm," *Conference on Applied Motion Control*, June 1987, pp.

[20] Hennessey, M., Priebe, J., Huang, P., and Grommes, R., "Design of a Lightweight Robotic Arm and Controller," *IEEE*. Ch2413-3/87.

[21] Pee, Myung-Ho "Control of a Flexible Manipulator Using a Linear Hydraulic Actuator," *Conference on Applied Motion Control*, June 1987, pp.

[22] Lees, J. K., "Advanced Composites Are Earning Their Wings," *Mechanical Engineering*, Vol. 110, No. 4, April 1988, pp. 50-53.

[23] Hastings, G.G., Dorsey, J., and Book, W.J. "Application of Balanced Realizations to Estimate Model Order Requirements for Flexible Manipulators," ASME, WAM, Boston, 1987.

[24] SUPERTAB User's Guide, Structural Dynamics Research Center, 1986.

[25] "Model Solution and Optimization," Structural Dynamics Research Center, 1986.

[26] Ewins, D.J., "Modal Testing: Theory and Practice," *Research Studies Press*, New York, Wiley, 1984.

[27] "Application Note 243-3," Hewlett-Packard Co., Palo Alto, CA, May 1986.

[28] "Application Note 243," Hewlett-Packard Co., Palo Alto, CA, Feb. 1985.

[29] Book, W.J., Maizzo-Neto, O., Whitney, D.E., "Feedback Control of Two Beam, Two Joint Systems with Distributed Flexibility," *Trans. of ASME. Journal of Dynamic Systems, Measurement, and Control.* 97, Sept. 1975, pp. 423-431.

[30] Cannon, Jr., R.H., and Schmitz, E., "Initial Experiments on the End-Point Control of a Flexible One-Link Robot," *Int'l Journal of Robotics Research.* 3(3),1984, pp. 62-75.

[31] Merritt, H.E., *Hydraulic Control Systems*, John Wiley and Sons, Inc., 1967. pp. 231-255.

[32] Singh, R.P., VanderVoort, R.J., and Likins, P.W., "Dynamics of Flexible Bodies in Tree Topology–A Computer Oriented Approach,"

[33] Turcic, D.A., and Midha, A., "Dynamic Analysis of Elastic Mechanism Systems, Part I: Generalized Equations of Motion," *Journal of Dynamic Systems, Measurement, and Control*

[34] Turcic, D.A., Midha, A., and Bosnik, J.R. "Dynamic Analysis of Elastic Mechanism Systems, Part II: Applications and Experimental Results," *Journal of Dynamic Systems, Measurement, and Control*

[35] Sadler, J.P. and Sandor, G.N., " A Lumped Parameter Approach to Vibration and Stress Analysis of Elastic Linkages," *Journal of Engineering for Industry. Trans. ASME.* Series B, Vol. 95, No. 2, May 1973, pp. 541-548.

[36] Sunada, W., and Dubowsky, S., "The Application of Finite Element Methods to the Dynamic Analysis of Flexible Spatial and Co-Planar Linkage Systems," *Journal of Mechanical Design*, Vol. 103, July 1981, pp. 643-651.

[37] Dubowsky, S. and Gardner, T.N., "Dynamic Interactions of Link Elasticity and Clearance Connections in Planar Mechanical Systems," *Trans. ASME, Mechanism Conf.*, New York, N.Y., Oct. 6-10, 1974.

[38] Chung, Ya-Chien, Lu, Shui-Shong, and Book, W.J., "Modeling and Optimal Control of a Lightweight Bracing Manipulator," *Journal of the Chinese Inst. of Engineers*, Vol. 10, No. 3, 1987, pp. 241-250.

[39] Lee, J.W., Huggins, J.D., and Book, W.J., "Experimental Verification of a Large Flexible Manipulator," to be presented at the American Control Conference, Atlanta, GA, June 13 - 17, 1988.

[40] Hughes, P.C., "Dynamics of a Chain of Flexible Bodies," *Journal of Astronautical Sciences*, Vol. XXVII, #4, Oct.-Dec. 1979, pp. 359-380.

[41] SMP Reference Manual, Inference Corporation, 1983.

[42] Sangveraphunsiri, V. "The Optimal Control and Design of a Flexible Manipulator Arm," Ph.D. Thesis, Georgia Institute of Technology, 1984.

[43] Data Translation Manual "MicroVMSLIB," Publication #sp0125 MicroVMSLIB V01.00, 1986.

[44] Oosting, K.,"Simulation of Control Strategies for a Two Degree-of-Freedom, Lightweight, Flexible Robotic Arm." Master's Thesis, Georgia Institute of Technology, May 1987.